Synsedimentary to early diagenetic rejuvenation of barite-sulfides ore deposits: Example of the Triassic intrakarstic mineralization in the Lodève basin (France)

D. Laurent, M. Lopez, P.-J. Combes, C. Guerrot, J.E. Spangenberg, E.C. Gaucher

Synsedimentary to early diagenetic rejuvenation of barite-sulfides ore deposits: Example of the Triassic intrakarstic mineralization in the Lodève basin (France)

D. Laurent[a*], M. Lopez[a], P-J. Combes[a], C. Guerrot[b], J.E. Spangenberg[c], E. C. Gaucher[d]

[a] Geosciences Montpellier, University of Montpellier, 34090 Montpellier, France

[b] BRGM/LAB, 45060 Orléans, France

[c] Institute of Earth Surface Dynamics (IDYST), University of Lausanne, Lausanne, Switzerland

[d] TOTAL-Scientific and Technical Center Jean Féger (CSTJF) – TOTAL, 64000 Pau, France

***Corresponding author:** Dimitri Laurent, present-day address: 20 rue du faubourg des trois maisons, 54000 Nancy, France.

E-mail address: dimit.laurent@gmail.com

Phone: +33 (0) 6 83 89 41 82.

Number of words of text (without abstract, bibliography and figure captions): 8632

Number of references: 89

Number of figures: 15

Number of tables: 2

Number of appendices: 1

Abbreviated title: Synsedimentary to early diagenetic rejuvenation of barite-sulfides ore deposits

Abstract

The exhumed Lodève Basin (Hérault, France) provides a rich suite of outcrops showing diagenetic Ba-Pb-Fe-Cu fronts trapped in karst system in Cambrian dolomites during the Triassic post-rift exhumation of the basin. The sedimentological analysis on 10 sites in the basin reveals that barites-sulfides fronts formed during humid-arid climate fluctuations and the emplacement of a shallow lake environment. The fabric of ore deposits, the microthermometry of fluid inclusions entrapped within barites and the strontium/sulfur isotopic compositions of barite-sulfides associations reveal two distinct groups of mineralizations, Type I and Type II, which are contemporaneous but resulting from different processes. The synsedimentary mineralization of the Type I, the presence of only primary single-phase liquid fluid inclusions within barite crystals and the gradual increase of $\delta^{34}S$ for both barites and chalcopyrites with depth (from -7 to +18.9‰ V-CDT) suggest ore precipitation close to the vadose zone under bacterial sulfate reduction (BSR) in a confined sulfate-rich playa lake aquifer. The similar $^{87}Sr/^{86}S$ ratios between barites and the overlying Triassic evaporites indicate that the barium and strontium derived directly from the overlying sulfate-rich lake. For the Type II, the high homogenization temperature of fluid inclusion entrapped within barite (modal Th between 60 and 80°C) and the association with hydrocarbon markers, confirm the participation of deeper basinal brines in addition to downward percolating sulfate derived from the lake environment. The high positive values of $\delta^{34}S$ for both barites and sulfides are typical of a precipitation linked to the combined action between anaerobic oxidation of methane and sulfate reduction (AOM-SR) at the sulfate-methane transition zone (SMTZ) during hydrocarbon migration. Similar $^{87}Sr/^{86}Sr$ ratios between Middle Triassic barites and previous Late Permian barites confirm that the source of metals precipitated at the SMTZ originated from the dissolution of anterior ore deposits located in the sulfate-depleted zone. This study links very shallow metallogenesis processes to reworking of MVT ore deposits by the action of sulfate-reducing bacteria around hydrocarbon seeps in a karstic environment.

Keywords: *karst; ore deposit; diagenetic barite; playa lake; sulfate reduction; fluid inclusions; sulfur and strontium isotopes.*

1. Introduction

A metallogenic cycle in a sedimentary basin can be summarized by four main key elements (Routhier, 1980): source, transport, deposition and remobilization of metals. If the three first steps are already well understood, the mechanism of remobilization needs to be better constrained. In particular, several questions remain concerning the nature of factors that control the redistribution of metals and its timing during the basin structuring (extension, compression, tectonic quiescence, etc...). If structural and stratigraphic controls are predominant in the formation of sulfur-rich sediment-hosted deposits such as Mississippi Valley-Type (MVT) or SEDimentary EXhalative (SEDEX) and often linked to the mature burial stage of sedimentary basin (topography-driven, sediment compaction, orogenic squeezing, overpressured reservoirs, thermal and density reflux drives; Leach et al., 2010), the rejuvenation of these ore deposits can occur during early diagenesis. In particular, barium-sulfides mineralization are known to form close to the sediment-water interface (SWI) due to metal remobilization (e.g. Torres et al., 1996; Riedinger et al., 2006). The cycle of barium is part of the debate about early diagenetic ore deposits rejuvenation, particularly linked to the formation of shallow diagenetic fronts related to the sulfate-methane transition zone (SMTZ) few meters under the SWI (e.g. Goldberg and Arrhenius, 1958; Brumsack, 1986; Torres et al., 1996). The SMTZ consists in a chemical boundary at the meeting place between downward diffusing sulfates coming from the overlying seawater and the upward circulating biogenic/thermogenic methane originated from deeper sources. This diagenetic transition results from a coeval activity of sulfate-reducing bacteria (bacterial sulfate reduction – BSR; Machel et al., 1995; Machel, 2001) and the methane-oxidizing Archaea (Anaerobic Oxidation of Methane – AOM; Reeburgh, 1976; Reeburgh, 1983) that consumes dissolved sulfates. Therefore, the SMTZ limits an underlying sulfate-depleted zone where primary barites are

79 dissolved (Barnes and Goldberg, 1976; Reeburgh, 1976; Borowski et al., 1999; Aloisi et al.,
80 2004; Rodriguez et al., 2000; Dickens, 2001; Niemann et al., 2006). The barium ions released
81 into the porewater then diffuse upward or can be moved with sedimentary brines along
82 permeable pathways (Kastner et al., 1990) up to a zone just above the SMTZ where SO_4^{2-} is
83 available, and precipitate to form authigenic barite-sulfides fronts (e.g. Torres et al., 1996;
84 Bréhéret and Brumsack, 2000; Aloisi et al., 2004; Arndt et al., 2006; Riedinger et al., 2006).
85 However, the role of SMTZ in the remobilization and precipitation of diagenetic barite-sulfide
86 fronts is only demonstrated in marine environment away from terrestrial influence, while
87 some continental depositional environments, such as playa lake, can led to similar chemistry
88 conditions. In addition, the major part of studies on SMTZ are mostly based on offshore 1D
89 core data (Torres et al., 1996; Aquilina et al., 1997; Riedinger et al., 2006; Snyder et al., 2007;
90 Borowski et al., 2013; Arning et al., 2015; Magnall et al., 2016; Hu et al., 2017) as very few
91 outcrop analogues have been evidenced that can give a 3D view of such shallow
92 metallogenesis (Zhou et al., 2015; Fernandes et al., 2017).
93 The continental Lodève basin contains several Ba-F-Cu-Pb-Fe ore deposits infilling karst
94 systems and fault zones affected Cambrian dolomites. Exceptional outcrop conditions allowed
95 to evidence a main mineralizing event during Late Permian syn-rift burial identified as a
96 MVT ore deposit (Laurent, 2015; Laurent et al., 2017). In addition, polymetallic deposits are
97 entrapped within meteoric karsts developed very close to the Middle Triassic post-rift
98 unconformity of the basin and sealed by evaporitic marls (Lopez, 1992). The question here is
99 whether the post-rift episode of barite and sulfide mineralization is related to a hydrothermal
100 fluid circulation, as for the Late Permian metallogenesis, or a diagenetic remobilization of the
101 previous ore deposits? We propose here a detailed study of the depositional environment and
102 karst dynamics during the post-rift mineralizing event supplemented by a multi-scale analysis

of textures, mineralogy, fluid inclusions and radiogenic/stable isotopes (sulfur and strontium) on mineralized markers. The objectives of this study will be to (i) constrain the link between the sedimentary infill of meteoric karsts and ore trapping (ii) define the diagenetic transformations, the different fluid events and associated stages of mineralization that follow the post-rift exhumation of the basin, and (iii) understand the origin of metals as well as the sulfur cycling in the system and its role in the timing and location of polymetallic deposits. *In fine*, this multidisciplinary approach allows us to propose an integrated model of economic metals trapping few meters below the SWI and to discuss the interconnection between karst dynamics, playa lake environment and hydrocarbon dysmigration.

2. Geological settings

2.1 Geodynamic evolution of the Lodève Basin

The Lodève Basin, located 50km northwestern of Montpellier in the south of the French Massif Central, is a 180 km² cuvette-shaped half graben (Fig.1A). The half-graben geometry of the basin is linked to a gravitational collapse along the Hercynian mountain chain from Late Carboniferous to Late Permian (Echtler and Malavieille, 1990). The series shows an overall 15-20° southward dipping continental infilling bounded in the south by a north dipping listric normal fault related to an inversion of a main thrust during the Late Hercynian collapse (Lopez et al., 2008) (Fig.1B). During this phase, the progressive tilting of the basin was accommodated at the hinge of the roll-over anticline by the development of an E-W trending synthetic and antithetic fault corridor (Lopez, 1992; Wibberley et al., 2007; Laurent et al., 2017; Fig.1A and 1B). Middle Triassic terrestrial deposits unconformably seal an erosive surface truncating both the Late Carboniferous-Permian half graben and its basement

at the southern and northern basin margins (Fig. 1B). This post-rift unconformity marked the end of the Late Hercynian tectonics followed by a major regional erosion during which at least 1500m of Permian deposits where eroded, representing a gap of 15Myr (Lopez, 1992; Laurent, 2015). The Mesozoic period corresponds to a major change of the tectonic regime with the opening of the South-East basin, where the Lodève area corresponds to the western continental high margin controlled by NE-SW trending faults. The complete sealing of the residual Paleozoic reliefs is then linked to the overall extension of shallow marine carbonate deposits during Jurassic. Jurassic series are today preserved on the Causse du Larzac plateau, which was uplifted during the Cenozoic with the regressive entrenchment of the river networks.

2.2 Stratigraphy of the Lodève Basin

The Hercynian basement

In the northern margin of the basin, the Stephano-Permian series onlap unconformably the large wavelength folded and partly thrusted Cambrian basement at the hinge point of the roll-over anticline (Lopez, 1992). The major part of the Cambrian deposits corresponds to thick massive dolomite interbedded with thin calcschist layers. These carbonates are intensively fractured and suffered a severe karstification and canyon entrenchment during the Late Hercynian subaerial exposure.

Syn-rift deposits (Stephano-Permian series)

The Stephanian sedimentary deposits, which are only visible in the westernmost part of the basin (Graissessac sub-basin) and evidenced at depth by older exploration drillholes (Lod 2 projected drillhole in Fig.1B), are composed of thick coarse alluvial fan deposits at the

base, passing upward to coarse fluvial sandstones and muddy swamp to peat clay formations. Above Stephanian series, the Permian deposits have been divided into two large megasequences: the Autunian Group and the Saxonian Group (Gand et al., 1997). The Autunian Group is composed of a 700m-thick isopachous series of deltaic sandstones evolving upward into deep anoxic lacustrine black shales with high potential source rock for hydrocarbon (Laurent, 2015) and interlayered with laterally continuous volcanic ash layers (Odin, 1986). The Saxonian Group lies unconformably on the Autunian deposits and displays a clear divergent pattern that marks the main southward tilting of the Hercynian basement along the south bordering listric fault. The thickness of the Saxonian Group is estimated to 3000m at present day but has certainly reached 5000m during the syn-rift subsidence of the basin (Laurent, 2015). It shows alluvial fan conglomerates passing rapidly to thick floodplain red pelites interbedded with thin blue-green playa lake mudstone deposits.

Post-rift deposits (Middle Triassic series)

The Middle Triassic deposits seal respectively the Permian in the southern and western part of the basin and the Cambrian and Precambrian basement in the northern part (Fig.2A and 2B). It consists of a 250m-thick pile composed of sandstone, mudstone and evaporite deposits, topped by mixed siliciclastic-carbonate facies at the transition with the Early Jurassic series. The series can be subdivided into four main formations according to their facies assemblage (Lopez and Mader, 1992; Fig.2C). The Lower Formation corresponds to the first 120m and shows typical Buntsandstein facies reported to the period from Anisian to Ladinian. It is mainly composed of fluvial sandstones passing to playa lake mudstone and evaporite deposits and vice-versa in a symmetrical megacycle. The Middle and Upper Formation (about 40m-thickness each one) show the same Keuper facies assemblage with a

175 basal 3-5 m-thick dolomite layer (key beds [a] and [b] in Fig.2C) capped by mudstones and
176 gypsum/anhydrite/dolomite interbeddings developed in shallow littoral sabkhas. The Rhaetian
177 Formation on top of the Triassic pile (Upper Norian) is characterized by mixed siliciclastic-
178 carbonate facies (Lower Unit in Fig.2C) passing upward to pure ooidal and bioclastic
179 grainstone-packstone deposits related to a shallow subtidal platform environment (Upper Unit
180 in Fig.2C).
181

182 **2.3 Metallogenesis of the basin**

183 The Lodève basin was the site of two episodes of barite-sulfide ore deposition, the first
184 during the Late Permian syn-rift structuring (Laurent et al., 2017) and the second following
185 the post-rift exhumation during the Middle Triassic. During the syn-rift phase, the Lodève
186 Permian basin experienced a long period of differential subsidence that led to a northward
187 basinal fluids migration at the interface between Cambrian dolomites and the Lower Permian
188 unconformity (Lopez, 1992; Laurent et al., 2017). Metal-rich dewatering fluids sourced in the
189 Autunian blackshales and ash layers and moved under thermal and pressure gradient below
190 the Early Permian seal to be accumulated at the hinge point of the roll-over anticline in the
191 northern part of the basin (Lopez, 1992; Laurent, 2015; Laurent et al., 2017). Fluids were
192 released and trapped along the active E-W compensation fault network, leading to
193 polymetallic barite-sulfide (Pb, Cu, Zn) veins in fault zone and paleokarst cavities (Lopez,
194 1992; Laurent et al., 2017). During Late Permian, the Autunian blackshales of the deepest part
195 of the basin reached the oil window and led to hydrocarbon migration according to the same
196 pathway and hydrodynamical conditions than prior metal-rich fluids (Laurent, 2015). Several
197 oil seeps are still visible at the contact between the Early Permian series and the Cambrian

198 basement (Lopez and Petit, 2003). This fluid event was characterized as a typical MVT ore
199 deposits linked to sediment dewatering during basin burial (Laurent et al., 2017).
200 Close to the post-rift unconformity marking the general exhumation of the entire basin,
201 different barite-sulfide deposits were identified in the rejuvenated Cambrian paleoreliefs
202 sealed by evaporitic marls in the northern part (Fig.2B and 2C; Lopez, 1992; Lopez, 1993).
203 These ore deposits which may result from a distinct mineralizing episode than the syn-rift
204 mineralizations are the focus of this paper.
205
206
207 **3. Materials and methods**
208 **3.1 Geological mapping and field studies**
209 The main work was conducted in the hanging wall of the Olmet normal fault on the
210 right bank of the Lergue River in the northern part of the basin where the lower formation of
211 the Middle Triassic onlaps unconformably the Cambrian basement (Fig.1, 2A and 2B). A de-
212 tailed geological map of the studied area was first carried out for the purpose of locating and
213 clarifying the main ore deposits and facies distribution along the major post-rift unconformity
214 (Fig.2A and 2B). Ten main ore deposits (identified by the name of the place and letter from a
215 to j in Appendix A) have been recognized and studied in this area. All these sites were care-
216 fully studied and sampled in order to characterize the lithology of the studied site, the sedi-
217 mentological assemblage and the fabric of the mineralized deposits. 4 main outcrops are de-
218 scribed in detail in this paper (in bold characters on Appendix A).
219 Complementarily, Triassic evaporitic gypsum and anhydrite were sampled at the near-
220 est accessible sites where this formation is accessible at outcrop (see Fig.1A for the location
221 of samples).

3.2 Petrography

Textures and mineralogy of ore deposits have been observed from polished thin sections using a Zeiss Scopa A1 optical microscope in transmitted and reflected lights at the University of Montpellier (France). These observations were supplemented by Scanning Electron Microscopy and Energy Dispersive X-ray Spectroscopy (SEM-EDS) with a FEI Quanta 200 Field Emission Gun of Schottky type.

3.3 Fluid inclusion microthermometry

Fluid inclusion microthermometry was performed on 100µm-thick double polished section using Linkam heating/freezing stage, mounted on a Leica microscope. The stage was calibrated according to synthetic fluid inclusions (Sterner and Bodnar, 1984) at temperatures of -56.6°C, 0.0°C and 374.1°C. The primary, pseudo-secondary and secondary nature of fluid inclusions assemblages were identified according to the criterion defined by Roedder (1984) and Bodnar (1985). In our study, only primary fluid inclusions were analysed reflecting the P/T/χ properties of the mineralizing fluids such as (i) the homogenization temperature (Th), (ii) the first apparent melting temperature at which liquids first co-exist with solids related to eutectic temperature (Te) and (iii) the final ice-melting temperature (TmIce), when solids completely disappeared. The McFlincor program (Brown, 1989) was used to calculate the salt composition, the salinity and the density of the initial fluids (Bodnar, 1993; Duan et al., 1992). Finally, fluorescence X and Raman spectroscopy were used to identify potential hydrocarbon-rich fluid inclusions.

3.4 Strontium concentration and isotopic composition

Strontium isotopic composition of barites has been measured at Isotope Laboratory of BRGM (Orléans, France). Around 30-50mg of barite powder was partly dissolved in beaker with a solution of 10ml of 8N HCl which was heated at 100°C during 12 days. After centrifugation, the liquid is separated from the solid residue and the latter is dried and weighted. 5 to 15% of barite was dissolved. The liquid is then evaporated to recover the dry residue then mixed up with 0.3ml of 41N HNO_3 and diluted with ultrapure water. Normalized on the Sr content in samples, 2µg of Sr was dried and submitted to the purification chain. A chemical separation is then performed with the purification of the Sr using an ion-exchange resin (Sr-Spec) before mass analysis according to a method adapted from Pin and Bassin (1992) (total blank <1ng). For the analysis of $^{87}Sr/^{86}Sr$ ratios, 150ng of Sr was loaded onto a tungsten filament with tantalum activator and analysed with a Finnigan MAT262 multi-collector solid source mass spectrometer. The internal precision obtained during the analyses is around ±10ppm ($2\sigma_m$) according to repeated analyses of the NBS987 standard to test the reproducibility, with a mean value of $^{87}Sr/^{86}Sr$ of 0.710246 ± 0.000010 (2σ, n = 18). Sample ratios are normalized to the certified value of the NBS987 ($^{87}Sr/^{86}Sr$= 0.710240).

The strontium concentration have been measured using the in situ laser ablation method LA-ICPMS (Laser ablation – Inductively Coupled Plasma Mass Spectrometry) on 100µm-thick double polished sections, at Geosciences Montpellier (France). We used a Compex 102 excimer laser (LambdaPhysik) operating in the deep-UV, which is periodically infilling by an ultrapure ArF gas excited by 28 kV electric shock in order to associate the fluor with argon to form the ephemerian molecule ArF. As this molecule is unstable, the liberation of fluor atom induced a photonic ray with a wavelength of 193nm. The particles issued from the interaction between the laser and the samples are directed to the ICP-MS torch by a He

flux and then mix to argon. The ablation by He enhanced the sensibility of the mass spectrometer and reduced the interelementary variations (Günther and Heinrich, 1999). The quantification of elementary concentration of samples was realized through the repeated measurements on a silicate glass (NIST 612) containing around 40ppm of most trace elements. The control of the accuracy and precision of the analyses was based on natural reference materials of BIR (basaltic glass) and artificial type of MACS3 (carbonate pellet). Signals are analysed by a magnetic sector mass spectrometer Element XR (Thermofinnigan). Finally, signal processing and concentration calculations were performed using GLITTER software (GEMOC – Van Achterbergh et al., 2001).

3.5 Sulfur isotopes

Sulfur isotopes analyses of barites, gypsum and anhydrite were performed at the Institute of Earth Surface Dynamics of the University of Lausanne (Switzerland) using a Carlo Erba 1108 elemental analyser (EA, Fisons Instruments, Milan, Italy) connected to a Thermo Fisher (Bremen, Germany) Delta V isotope ratio mass spectrometer (IRMS) that was operated in the continuous helium flow mode via a Conflo III split interface (EA-IRMS). The stable isotope composition of sulfur is reported in the delta (δ) notation as the per mil (‰) deviation of the isotope ratio relative to known standards: $\delta = [(R_{sample} - R_{standard})/R_{standard}]x1000$, where R is the ratio of the major heavy to light sulfur isotopes ($^{34}S/^{32}S$). The sulfur standard is the Vienna Cañon Diablo Troilite (V-CDT). Preparation of samples have been made according to the method presented in Spangenberg et al. (2010). The reference SO_2 gas was calibrated against the IAEA-S-1 sulfur isotope reference standard (Ag_2S) with $\delta^{34}S$ value of -0.3‰. The overall analytical reproducibility of the EA-IRMS analyses, assessed by replicate analyses of three laboratory standards (synthetic cinnabar, with

293 a working $\delta^{34}S$ value of +15.5‰; barium sulfate, +12.5‰; pyrite Ch, +6.1‰; pyrite E, –7.0‰)
294 is around ±0.2‰ (1 SD). The accuracy of the ^{34}S analyses was checked periodically by
295 analyses of the international reference materials IAEA-S-1 and IAEA-S-2 silver sulfides (0.3‰
296 and +22.7 ±0.2‰, respectively, values from IAEA-Catalogue and Documents) and NBS-123
297 sphalerite (+17.09 ±0.31‰, value from NIST-Catalogue and Documents).
298 In addition, in situ sulfur isotope measurements on 23 chalcopyrites were made by
299 Secondary Ion Mass Spectrometry (SIMS) equipped with a cesium source on CAMECA
300 IMS5F at the University of Montpellier (France). The internal precision as well as the
301 reproducibility of results was checked on laboratory standards of three chalcopyrites whose
302 $\delta^{34}S$ signatures are respectively 4.4 ±1.6‰, 3.47 ±0.42‰ and 2.29 ±0.2‰, giving an
303 analytical error inferior to ±1‰.
304
305
306 **4. Results**
307 **4.1 Architecture, mineralogy and texture of Middle Triassic ore deposits**
308 **4.1.1 The Roche Percée paleo-pothole**
309 The site of Roche Percée is located close to the right bank of the Soulondres River in
310 the western suburb of Lodève city (b in Fig.2A and Appendix A). The outcrop consists of an
311 isolated dyke of mineralized and silicified breccias, largely exhumed from the surrounding
312 rocks, and rooted into the Cambrian basement. Here the Triassic cover has been totally erod-
313 ed.
314 The mineralized dyke displays a subvertical east-west trending wall of 40 m-long, 4m-
315 wide and 8 to 12m-high entrenched parallel to the stratigraphic contact between beige massive
316 dolosparite in the southern border and blue-grey calcschists in the northern side (Fig. 3A).

317 The dyke infill is bounded by a silicified wall penetrating both the Cambrian dolomites and
318 the calcschists on a thickness of about 10 to 20cm and even reaching 4m in the northwestern
319 slab (Fig. 3B and 3C). Moreover, angular centimetre to pluri-decimetre-size blocks of silici-
320 fied wall are visible in the dyke infill, indicating that the major stage of silicification preceded
321 the mineralization. Three main facies, called respectively RP1, RP2 and RP3, have been ob-
322 served in the dyke infill:

323 **- RP1 Facies:** this facies consists of a black organic matter- and silica-rich pyrite bear-
324 ing mudstone forming the northward inclined slab in the northwestern part of the outcrop
325 (Fig. 3A and 3B). This facies is thinly laminated with lighter fine siltstone laminae alternating
326 with dark organic-rich and highly silicified mudstone laminae;

327 **- RP2 Facies:** composing the main dyke infill, the RP2 Facies is a well stratified pluri-
328 centimetre- to decimetre-thick barite-rich beige siltstone forming undulated bedsets with mul-
329 tiple low-angle truncations (Fig.3B, 3C, 4A and 4B). Perpendicular sections of the dyke show
330 a clear concave shape pattern of the bedsets attesting to a collapse during the phase of infil-
331 ling. In thin section, the RP2 Facies shows a particularly remarkable stacking of millimetre- to
332 centimetre-thick graded couplets including a silt and sand-size grains with discrete barite
333 crystals plates, passing upward to brown dolomitic siltstone (Fig.4C). Barite plates are often
334 broken and corroded (Fig.4D). Plates are progressively more abundant to the top forming
335 massive barite laminae of millimetre- to centimetre-size fibro-radiated spherules. Locally,
336 speckles and blebs of galena, chalcopyrite and gray copper are dispersed in barite (Fig.4E).

337 **- RP3 Facies:** the RP2 Facies is overlaid or passes laterally to massive mud-supported
338 breccia, composing the RP3 Facies (Fig.3B and 3C). The breccia consists in centimetre- to
339 pluri-decimetre size angular clasts of calcschists, dolomites and silicified surrounding rocks
340 floating into barite-rich siltstone to fine sandstone (upper part of Fig.4A). In some places, both

341 the RP2 and RP3 Facies display centimetre-size craters linked to gypsum-anhydrite dissolu-
342 tion (Fig.4A).
343
344 **4.1.2 The Olmet Road paleo-lapiaz network**
345 Along the Olmet Road (f in Fig.2A and Appendix A), an outcrop consists in a fault-
346 controlled Cambrian paleorelief partly onlapped by sandstones and marls belonging to the
347 Lower Formation of the Middle Triassic (Fig.2C and 5A). The main outcrop forms an
348 irregular 2.5 to 6m-high and 45m-long ENE-WSW trending escarpment. The vertical
349 succession shows in the upper part of the outcrop massive to roughly bedded Cambrian
350 dolomites with a general dip of about 80° to the south, unconformably onlapped by bluish
351 evaporitic marls and fine to very fine yellowish sandstones moulding the karstified paleorelief
352 (Fig. 5A). The intermediate part of the outcrop is characterized by a blurred and very irregular
353 orange to dark brown colored interval partly masking the surface of unconformity because of
354 the intense impregnation by limonites, goethite and hematite. This oxidized front has a
355 thickness ranging from about 1 to 4m according to the depth of karstification. Careful
356 observation of this interval shows that the beige-colored Cambrian dolosparites progressively
357 assumes upward a brown color with an increase in iron carbonate and silica content. In
358 parallel to paleo-lapiaz infill, silicified sulfide-impregnated subvertical bed-controlled bands
359 develop locally several meters below the paleosurface. The western part of the outcrop is
360 crossed by a NW-SE trending normal fault showing a throw of about 4m toward the North-
361 East.
362 Barite-sulfides mineralizations are covered by alternations of bluish gypsum-rich
363 marls and fine partly silicified sandstones (Fig.5A and 5B). Three types of mineralizations
364 have been observed below the unconformity surface, from the base of the outcrop to the

365 paleosurface: (i) pluri-centimetre-thick massive barite veins, without sulfides, dispersed in the
366 Cambrian dolomites with a random distribution; (ii) connected to the paleosurface, subvertical
367 pluri-decimetre-thick partly oxidized bed-parallel pyrite veins and sulfide-rich impregnations
368 of the Cambrian dolomites (Fig.5B); and (iii) the main ore facies consists in a complete
369 mineralized sedimentary infill all along the irregular karstic paleosurface affected by paleo-
370 lapiaz. In the central part of the outcrop, this main ore facies forms a laminated sulfide-rich
371 bluish vadose silty claystone including brown patches of iron oxides associated with barite
372 pockets (Fig.5A and 5C). This mineralized interval is capped by a 1m-thick brown sulfide-
373 rich siltstone to very fine sandstone, partly silicified sealing the karstic Triassic unconformity.
374 This facies is several meters-thick and fills completely the karstic cavities in the eastern and
375 western part of the outcrop. The mineralized suite include dispersed blebs and speckles of
376 galena, sphalerite and grey copper filling the intergranular porosity and forming thin veins or
377 platings associated to secondary copper and lead carbonates, barite and bitumen blebs. As this
378 facies is really representative to the Middle Triassic mineralizing event, we name this deposit
379 OR Facies in the following.
380
381 **4.1.3 The Montifort Road planar cavities string**
382 This ore deposit is located along the Montifort road to Olmet village in the south sub-
383 urb of Lodève city (a in Fig.2A and Appendix A). Here the Cambrian blue-grey calcschists
384 dip 75° to the south and are unconformably covered by the Middle Triassic deposits (Fig.6A).
385 The Triassic unconformity is clearly irregular with decimetre-large potholes sealed in onlap
386 by very fine brown sandstones and evaporitic marls interbeddings. About 1 to 1.5m below the
387 unconformity, the calcschists are intersected by superposed strings of interconnected planar
388 cavities parallel to the unconformity surface and partly filled with barite and brown fine

grained silts (Fig.6A and 6B). The size of the planar cavities is comprised between a few centimetre to a few decimetre. They are surrounded by a sub-vertical fracture network developed in bedding planes, enlarged by karstification process and sometimes infilling by vadose sediments. As observed in the Roche Percée paleo-pothole, the planar cavities string and associated veins are accompanied by an intense silicification of the surrounding calcschists penetrating the walls from about 10 to 20cm with red-coloured chalcedony development (4 in Fig. 6B). The planar cavities display a geopetal fabric with carbonate granules and siltstone sealed locally by barite blocky cement (Fig. 6C and 7AD). The granules infilling the cavities show a particularly relevant reverse grading with a size ranging from 100µm at the base to a few millimetre at the top (Fig. 6B and 6C). Granules are rounded and composed of dolomudstone-supported silts (Fig.7A). Laterally within the infilling, granules pass to more homogeneous sediments constituting mud with curved cracks. In thin section, the fine-grained sediment and associated granules are mainly composed of dolomudstone-supported silt including quartz and iron oxides. Very fine-grained silt (20 to 100µm) partly fills the intergranular space with a geopetal pattern. On cross polarized light microscopy, the granules show a partial penetrative silicification with the development of quartzine spherolites tending to evolve into microquartz (Fig.7A). The residual intergranular voids are upholstered with drusy megaquartz that can close completely the remaining space (Fig.7B).

The barite and accessory sulfide cement developed discontinuously above the granule-siltstone infill. The contact is erosional with a very irregular sharp and underlined by pluri-millimetre-thick brown ankerite (Fig.6C, 7B, 7C). This mineralized facies is mentioned as MR1 Facies in the following. Fluorescence X observations reveal a high content of organic matter-rich patches within and along crystal faces of ankerite at the contact with barite crystals (Fig.7D). Locally, the intrakarstic sedimentary infill is brecciated and incorporated as re-

413 sidual clasts or blocks in the barite cement. The barite develops as fan shaped cockade clus-
414 ters corresponding to the growing of large slats in an open space (Fig.6C and 7C). Close to the
415 contact with barites, pyrites, galena and sphalerite patches are present, always cemented by a
416 late sparitic calcite (Fig.9E) and often associated with bitumen bubbles and blebs trapped in
417 residual voids.

418 Two hundred meters north-eastward along the main road, the Cambrian dolomites are
419 unconformably onlapped by the basal conglomerate of the Early Permian dipping 25° to the
420 North (outcrop j on Fig.2A and Appendix A). The conglomerates are themselves capped hori-
421 zontally by the Middle Triassic sandstone and marl alternations. Here the Cambrian dolomites
422 and basal conglomerates are crossed by multiple barite and grey copper/chalcopyrite veins
423 and hydraulic breccia without any link with the overlying Triassic unconformity. This miner-
424 alized fabric, called here as MR2 Facies, is similar to the Late Permian MVT ore deposits de-
425 scribed by Laurent et al. (2017).

426

427 **4.1.4 The Belbezet karstic mine**

428 This site corresponds to an old mining work exploited during the roman period for
429 copper and silver. The main mining gallery is carved in the mineralized interval along the
430 basal unconformity on the flank of a paleorelief between the Cambrian dolomites at the
431 footwall and a debris-flow conglomerate at the hanging wall (e in Fig.2A, Fig.8A and 8B).
432 The stratigraphical contact shows a general dip of about 35° to the South-West. The debris-
433 flow conglomerate is about 2m-thick and includes numerous pebble-sized dolomite blocks
434 floating into a sandy matrix. It is capped by blue-green marls alternating with thin very fine
435 sandstone layers including pseudomorphs after anhydrite. The paleosurface includes metric
436 paleo-potholes associated with an open-fracture network descending several decimetres to

437 several meters below the unconformity and including pluri-decimetres blocks brecciated in
438 situ and intrakarstic infill.

439 The mineralized interval (BM Facies) fills the cavities network with a very variable
440 thickness. It is composed of sulfide-barite-rich silty-clayey matrix packing within
441 heterometric Cambrian blocks (Fig.8B and 8C) and passing upward to massive white barite
442 (Fig.8A and 8B). Barites are locally highly sheared and also injected by grey copper sulfides,
443 chalcopyrites and abundant bitumen droplets and heavy oil that totally stain the barite in grey
444 (Fig.8D).

445

446 ## 4.2 **Fluid inclusion petrography and microthermometry in barites**

447 ### **4.2.1 Petrography of fluid inclusions**

448 The fabric of primary fluid inclusions in barite within the MR2 Facies, from the
449 northern part of the Montifort Road outcrop, displays a two-phase assemblage with an oblong
450 geometry positioned along growth zones and a size between 10 and 40µm. We have
451 intentionally excluded fluid inclusions close to the cleavage planes as barite is very sensitive
452 to post-crystallization deformation (Ulrich and Bodnar, 1988). The Rv (ratio between vapor
453 and vapor+liquid) is ranging between 10 and 20%.

454 Entrapped within blocky barites of the MR1 Facies from the Montifort Road planar
455 cavities string, we observed two generations of primary fluids inclusions: two-phase
456 inclusions with Rv of 20 to 30% close to the centre of the crystal and stable single-phase
457 liquid inclusion along the external face (Fig.9A). Secondary inclusions are also identified with
458 a higher Rv, between 50 and 60%, a larger size, and evidences of post-trapping deformation
459 such as necking-down. Very few and small hydrocarbon-rich fluid inclusions were identified
460 by fluorescence X despite the fact that oil and bitumen is clearly visible in the mineralized

461 facies. Raman analyses were not discriminating, because of the high fluorescence of the
462 samples linked to the important content of oil impregnations in barites.

463 Fluid inclusions entrapped within the rhythmic infilling of the Roche Percée paleo-
464 pothole (RP2 Facies) and the barite from the Olmet Road paleo-lapiaz (OR Facies) are
465 essentially stable single-phase liquid inclusions and very small in size considering the fine
466 barite crystallites (Fig.9B). Even during cooling of samples, no gas bubbles have nucleated in
467 these inclusions. Consequently, no microthermometry have been performed on these
468 mineralized facies.

469

470 **4.2.2 Microthermometry**

471 The results of microthermometry (Te, TmIce and Th) for all selected ore facies are
472 presented on Table 1 and Figure 10.

473 The primary fluid inclusions in the MR2 Facies of Montifort Road show a majority of
474 homogenization temperatures in the range of 180-200°C. The Te are between -30 and -20°C,
475 for an average of -24°C, indicating that the mineralizing fluid is an H_2O-NaCl brine with a
476 low proportion of Ca^{2+} (from -22.9°C: Crawford, 1981; from -21.2°C: Borisenko, 1977). The
477 TmIce are characterized by a wide distribution of values for an average of -8.77°C,
478 corresponding to a salinity of 12.6 wt%eq.NaCl (Brown and Lamb, 1989) and a density of
479 0.987 (Bodnar, 1994).

480 For the MR1 Facies within the Montifort Road planar cavities string, primary two-
481 phase inclusions have lower homogenization temperatures, mostly in the range of 60 to 80°C
482 for a mean value of 77°C. The modal values of Te and TmIce are between -25/-20 °C and -
483 12/-10°C respectively, corresponding to an average salinity of 13.56 wt% eq.NaCl and a
484 density of 1.069.

485

4.3 Sulfur and strontium geochemistry

487 Strontium concentration and strontium isotopes ($^{87}Sr/^{86}Sr$) analyses on barite of the
488 three main textural facies (RP2, MR1 and BM) were performed associated to sulfur isotopes
489 ($^{34}S/^{32}S$) measurements on both barites and chalcopyrites evidenced within a same facies.
490 Similar sulfur isotopes analyses have been made on chalcopyrites in a fourth sample of
491 mineralization from the Olmet Road (OR Facies) and also in evaporites belonging to the
492 Middle to Upper Triassic formations (EV1 and EV2 Facies). A comparison with the isotopic
493 signatures of Late Permian barites and sulfides presented in Laurent et al. (2017) was also
494 carried out in order to determine a potential geochemical inheritance (Table 2).

495

4.3.1 Ba-Sr concentration and strontium isotopes in barites

497 The Sr concentration in barites close to the Triassic post-rift unconformity ranges from
498 4400 and 11800ppm, far away from the barites attributed to the Late Permian in Laurent et al.
499 (2017) that ranges from 19500 to 43803ppm (Table 2).

500 Figure 11 shows the $^{87}Sr/^{86}Sr$ values as a function of strontium concentration for
501 Middle Triassic barites compared to the signature of the three ore generation of Late Permian
502 barites identified in Laurent et al. (2017). The strontium isotopic signature of the barites
503 composing the RP2 Facies is significantly lower than all other barites with a value of 0.70888,
504 but very close to the general value of Triassic evaporites which ranges between 0.70745 and
505 0.70795 after Koepnick et al. (1990) and up to 0.7086 after Song et al. (2015). The $^{87}Sr/^{86}Sr$
506 values between 0.71139 and 0.71142 for BM and MR1 Facies respectively are close to the
507 signatures of the first and second generations of Late Permian barites.

508

4.3.2 Sulfur isotopes of barites, chalcopyrites, evaporitic gypsum and anhydrite

As chalcopyrites are often associated with barites in all ore facies studied in this paper, we use the difference of $\delta^{34}S$ between barite and associated chalcopyrites in a same facies $\delta^{34}S_{barite}$ - $\delta^{34}S_{chalcopyrite}$, annotated $\varepsilon^{34}S$, which may be representative of the fractionation of sulfur isotopes during the precipitation of the barite-sulfide front. All results of sulfur isotopic composition are synthetized in Table 2.

We obtained values of $\delta^{34}S$ of +13.7 and +14.79‰ V-CDT for the Triassic evaporitic gypsum (EV1 Facies) and of +14.6 and +14.9‰ V-CDT for the Triassic evaporitic anhydrite (EV2 Facies).

For the Middle Triassic barites, the $\delta^{34}S$ of OR and RP2 Facies ranges between +15.7 and +16.2‰ V-CDT and are slightly superior for the mineralizations corresponding to the MR1 and BM Facies with $\delta^{34}S$ values between +16.2 and +18.5‰ V-CDT. For all Middle Triassic barites, $\delta^{34}S$ values are higher than the Triassic evaporites but mostly similar to the Late Permian barites which signatures range between +15.6 and +18.4‰ V-CDT (Laurent et al., 2017).

The $\delta^{34}S$ for Middle Triassic chalcopyrites is different from Late Permian sulfide deposits ($\delta^{34}S$ between -15 and -5‰ V-CDT; Laurent et al., 2017) with two distinctive domains:

(i) negative $\delta^{34}S$ values for RP2 and OR Facies, ranging respectively from -2.1 to -1.4‰ V-CDT and from -7.2 to -1.7‰ V-CDT. For these facies, the difference of $\delta^{34}S$ between barite and chalcopyrites $\varepsilon^{34}S$ ranges between +17.1 and +23.4‰ V-CDT, representing an important fractionation of sulfur isotopes during the precipitation.

(ii) positive $\delta^{34}S$ values in BM and MR1 Facies. The BM Facies shows $\delta^{34}S$ varying between +11.9 and +17.1‰ V-CDT, close to the Triassic evaporites signatures, and are characterized by a very week $\varepsilon^{34}S$ ranging from +4.8 to -0.9‰ V-CDT. The MR1 Facies has a

533 $\delta^{34}S$ of +18.9‰ V-CDT, for a $\varepsilon^{34}S$ of -0.4 and -2‰, thus close to 0‰ if we consider the ana-
534 lytical error of around 1‰ for SIMS measurements.

535 Even though some chalcopyrites are considered to be synchronous with barites accord-
536 ing to the petrographic study, we did not consider an isotopic equilibrium between these two
537 phases. Indeed, the temperatures calculated according to the Rye and Ohmoto (1974) and
538 Ohmoto and Lasaga (1982) equations give aberrant precipitation temperature values (superior
539 to 250°C) in comparison with those obtained by microthermometry.

540

541

542 **5. Discussion**

543 **5.1 Timing and origin of mineralizaing fluids**

544 Field observations supported by fluid inclusions microthermometry and
545 sulfur/strontium isotopes analyses clearly indicate two main types of mineralization trapped in
546 the Cambrian paleokarst just below the Middle Triassic unconformity (Fig.11).

547 The early mineralization includes anhedral sulfides (pyrite, chalcopyrite, galena and in
548 less proportion sphalerite and tetrahedrite) that precipitated into void spaces of sheaf-like and
549 massive barite composing the intrakarstic sediments of the Roche Percée paleo-pothole (RP2
550 and RP3 Facies) and of the exokarst observed in the Olmet Road outcrop (OR Facies). The
551 alternation of barite and intrakarstic sediments in karstic cavities and the presence of
552 allochtonous corroded and broken barite crystals in the RP2 Facies indicates their
553 synsedimentary precipitation origin and hydrodynamic transportation during water table
554 fluctuation in the karst. For convenience, we named this event Type I mineralization.

555 A second type of barite-sulfides deposits has been observed associated with
556 hydrocarbon and mineralized few meters below the water table in endokarst network. They

were particularly observed at the Montifort Road outcrop and Belbezet Mine and include euhedral sulfides (pyrite, chalcopyrite and galena) trapped into cockade-shaped barite for the first area (MR1 Facies) and disseminated into a silty clayey matrix from the second zone (BM Facies). The ore deposits related to this event is called Type II mineralization.

Complementarily, the barite of the MR2 Facies, sampled in a sub-vertical vein distant from the post-rift unconformity, are characterized by higher homogenization temperature (between 139 and 195°C) of primary fluid inclusions than for the Type I and Type II mineralizations (between 49 and 102°C) (Fig.10 and Table 1). Such fluid characteristics are very similar to the ore facies described for the Late Permian MVT episodes by Laurent et al. (2017). Consequently, we attributed these veins as a prior mineralizing event regarding the Middle Triassic mineralizing episodes.

Knowing that strontium isotopes do not fractionate below 400˚C (Matter et al., 1987), the $^{87}Sr/^{86}Sr$ of barites reflects the strontium isotopic composition of the source. In our case, strontium isotopic signatures suggest two different sources of metals for Type I and Type II mineralizations (Table 2 and Fig.12). The $^{87}Sr/^{86}Sr$ value of 0.70888 of barites of the Type I in the Roche Percée paleo-pothole (RP2 Facies) is compatible with the direct participation of Sr and associated Ba derived from the underlying Middle Triassic playa lake aquifer as the signature is very similar to Triassic evaporites ($^{87}Sr/^{86}Sr$ between 0.70745 and 0.70795 after Koepnick et al. (1990) and up to 0.7086 after Song et al. (2015)). This direct connection between the karst and the overlying depositional environment is also supported by the synsedimentary features of mineralizations. On the contrary, the strontium isotopic signatures of barites at the Belbezet Mine and Montifort Road outcrops (BM: $^{87}Sr/^{86}Sr$ of 0.71139; MR1: $^{87}Sr/^{86}Sr$ of 0.71142), constituting the Type II mineralizations, are much more radiogenic than

580 Triassic evaporites (Fig.12) which preclude a direct link with the sulfate-rich lake waters and
581 rather suggest an external source of metals.

582 In the MR1 Facies, the high Th of fluid inclusions in barites, between 42 and 102°C,
583 and an elevated salinity (Fig.10), do not correspond to an early diagenetic stage close to the
584 SWI and necessarily involved the migration of deep basinal brines. The involvement of
585 basinal brines is supported by the systematical association of barites of the Type II and
586 hydrocarbon markers indicating that the petroleum system was still active during the Middle
587 Triassic. However, if the barite crystal initiated during deep basinal fluid migration, the
588 presence of single-phase liquid inclusion in the late stage of barite growing suggests that the
589 crystal development finalized within a low-temperature water (Goldstein and Reynolds, 1994).
590 Even if, the presence of oil in the Type II mineralization could indicate that the Middle
591 Triassic metallogenesis may be a simple continuation of the previous Late Permian fluid
592 migration (Laurent et al., 2017), we suggest that both episodes are decoupled. The cessation
593 of fluid migration linked to the 1500m post-rift exhumation of the basin margin during the
594 Middle Triassic (Lopez, 1992; Lopez et al., 1998; Laurent, 2015) is supported by the different
595 strontium isotopic signature between Middle Triassic barites and the latest generation of the
596 Late Permian Barites (Fig.12) (Laurent et al., 2017). The $^{87}Sr/^{86}Sr$ of the Type II barites are
597 very close to the barites associated with the first and second Late Permian fluid events
598 occurring in the Lodève Basin (Laurent et al., 2017) suggesting that metals for Type II
599 mineralizations were derived from the remobilization of previous barite-sulfide mineralization.
600 In addition the drastic decrease in the Sr concentration in the Middle Triassic barite (Fig.12) is
601 typical of the leaching of anterior barites by undersaturated water (Gordon et al., 1954; Cohen
602 and Gordon, 1961; Renault and Brower, 1971).
603

5.2 Ore trapping redox conditions

As demonstrated previously, strontium isotopic signatures of Type I barites confirm that the most valuable source of sulfur is the playa lake environment linked to semi-arid climate conditions. The high sulfur isotopes fractionation between Type I barite-sulfide deposits and the Triassic evaporites may indicate a process of BSR (Machel et al., 1995). In this case, we assumed that dark organic-rich facies infilling karstic cavities at the Roche Percée paleo-pothole (RP1 Facies) and local abundance of plants and wood debris in the basal debris-flow deposits at the Belbezet Mine could represent the source methane, necessary to bacteria metabolism. The presence of only primary single-phase liquid fluid inclusions indicates low-temperature precipitation, below 50°C (Goldstein and Reynolds, 1994) (Table 2), compatible with the BSR reaction which is stopped around 80°C (Postgate and Schwartz, 1985). The high values of the $\varepsilon^{34}S$, between 17.1 and 23.4‰ V-CDT (Fig.13 and 14), is consistent with the process of BSR development in a closed-system for sulfate supply (Harrison and Thode, 1958; Ohmoto, 1990; Canfield, 2001; Wortmann et al., 2001; Lerouge et al., 2011).

In the case of the Type II mineralization (MR1 and BM Facies), the $\delta^{34}S$ of sulfides show an important ^{34}S enrichment with $\delta^{34}S$ reaching the value of Triassic evaporites and synchronous barites (Fig.13 and 14). High values of $\delta^{34}S$ in sulfides in a low temperature sulfate-rich environment are generally attributed to the development of a SMTZ associated with a process of anaerobic oxidation of methane coupled with bacterial mediated sulfate reduction (AOM-SR). As explained in the introduction, the SMTZ is a redox boundary resulting from the coeval activities of sulfate-reducing bacteria and anaerobic methanotropic Archaea (Reeburgh, 1976; Alperin et al., 1988; Hoehler et al., 1994; Borowski et al., 1997; Borowski et al., 1999; Aloisi et al., 2000; Dickens, 2001; Niemann et al., 2006; Knittel and Boetius, 2009). At

628 the depth of SMTZ, AOM is responsible for the production of a significant amount of dis-
629 solved HS^- and because the interstitial sulfate is really enriched in ^{34}S at this depth, the reac-
630 tion between dissolved sulfur and metals results in the precipitation of ^{34}S-rich sulfides com-
631 pared to sulfides in the overlying sulfate reduction zone which is submitted to BSR, as it is the
632 case for the Type I mineralization. A crucial element in our study area is the migration of hy-
633 drocarbon contemporaneous to the Type II mineralizations. Consequently, we assume that, at
634 the time of a permanent shallow lake environment, a downward diffusion of sulfates toward
635 the karst network and the rise of deep hydrocarbons in the Cambrian basement were condu-
636 cive to the formation of a SMTZ (Fig.14). The undersaturation in SO_4^{2-} below the SMTZ
637 caused the dissolution the Late Permian barite-sulfide deposits thus constituting the main
638 source of sulfate and barium for the Type II mineralizations, as also demonstrated by the simi-
639 lar strontium isotopic signature between Type II and Late Permian barites. When hydrocar-
640 bons reached the SMTZ, the increase of alkalinity in the solution caused the formation of au-
641 thigenic carbonates (Moore et al., 2004; Raiswell and Fisher, 2004; Meister et al., 2007) as
642 evidenced by the hydrocarbon-rich ankerite minerals systematically surrounding the mineral-
643 zations in the endokartic cavities. Neo-formed barite forming at SMTZ is not so ^{34}S-enriched
644 compared to Triassic evaporites and the $\varepsilon^{34}S$ is consequently very low (Fig.13 and 14). The
645 weak sulfur isotopes fractionation between sulfides and sulfates at SMTZ have been already
646 demonstrated for diagenetic fronts developed close to the seafloor and is the consequence of
647 an open system for sulfate supply (Jørgensen et al., 2004; Borowski et al., 2013; Magnall et
648 al., 2016).

649 We saw that the precipitation of Type I and Type II can happened in distinct condi-
650 tions in terms of sulfate availability (open versus closed systems) that led to a different evolu-
651 tion of sulfur isotopic composition for the respective barite-sulfide deposits. Type I minerali-

652 zation was clearly associated to a shallow BSR during periodical sulfate-rich water percola-
653 tion from ephemeral playa lake occurring during the first step of the onlap of Middle Triassic
654 sediments (Fig.14). This configuration thus provided a limited quantity of sulfate. On the con-
655 trary, Type II mineralization reveals early burial conditions with an ore trapping in the karst
656 controlled by the convergence of a permanent downward sulfate flux from the overlying
657 evaporitic lake and the upward migration of deep hydrocarbon forming the SMTZ (Fig.14).
658 Perennial supply of sulfates for the Type II mineralization, defining the "open system", is
659 probably governed by the seal capacity for downward fluids at the unconformity surface. In
660 the case of Belbezet Mine and Montifort Road, the paleokarst surface is covered by thick
661 conglomerate and sandstones respectively, both lithologies favoring the continuous percola-
662 tion of the sulfate-rich water during the burial of the series. On the contrary, in the case of the
663 Olmet Road, the direct sealing of the paleokarst system by a thick marly cover could explain
664 the isolation during burial and the lack of Type II mineralization.
665
666
667 **5.3 Genetic model for synsedimentary to early diagenetic ore deposits**
668 The two distinct ore trapping mechanisms evidenced in this work during the Middle
669 Triassic period of the Lodève Basin allow us to propose a conceptual model of synsedimen-
670 tary to early diagenetic ore deposits. This model presents the interconnection of sedimentary
671 basin geodynamics, meteoric karst evolution and migration of deep basinal hydrocarbon-rich
672 fluids in the development of very shallow barite-sulfides deposits. Three main stages can be
673 distinguished (Fig. 15):

(i) Stage 1: Intense weathering and epigenetic karstification after the post-rift exhumation of the basin

After the Permian rifting of the Lodève basin, a significant base level drop of about 1500m, resulting from a general uplift of the margins during the initiation of the Tethys-Ligure basin opening (Lopez, 1992), caused the widespread erosion of the Late Permian sedimentary deposits and the differential exhumation of the Hercynian basement (Fig.15 – Stage 1). All the studied outcrops show precisely the base of the Middle Triassic pile onlapping a well define paleokarstic surface characterized by paleolapiaz, potholes and exo- and endokarstic cavity networks. At the Roche Percée ore dyke, relevant withdrawal structures and collapse fabric indicate a mechanism of karstification associated to *per descensum* sedimentary infilling of a major deep paleo-pothole developed along a vertical permeability barrier between the calcschists and the dolomites. Exokarstic processes prior to the deposition of Middle Triassic basal formation is also well-observed along the Olmet Road with the development of paleo-potholes and weathering markers along the Middle Triassic paleosurface. In addition, the Montifort Road outcrop reveals the strings of interconnected planar cavities which indicate endokarstic dissolution processes at the front of a fluctuating water table, prior to or just at the beginning of the deposition of the first Middle Triassic sediments. During the dissolution of the surrounding calcschists, the insoluble fraction including silt-sized quartz and iron oxides was accumulated in the cavities and conduits forming typical vadose silt deposits with granules. Such micro-nodular pedogenic granules were also described in the Late Cretaceous-Early Tertiary of the southern France by Plaziat and Freytet (1978) with possible reverse grading reported to the development of pseudo-microkarst (Freytet and Plaziat, 1978, 1982; Hay and Wiggins, 1980; Alonso-Zarza, 2003). In this case overlapping of pedogenic, vadose and shallow phreatic processes led to the

698 granification of sediments (Mazzullo and Birdwell, 1989) controlled by periodical changes in
699 the position of the water table (Alonso-Zarza, 2003). This stage corresponds to the formation
700 of the karst trap for later mineralizations.
701
702 *(ii) Stage 2: Alkaline stage during the playa lake initiation*
703 The silicification strengthening the walls of the Roche Percée ore dyke occurred
704 before the main karstic infilling, partially plugging the karstic paleosurface of Montifort Road
705 and Belbezet Mine (Fig.15 – Stage 2). Silica came from the partial leaching of the quartz silt-
706 fraction dispersed in the basement from the exokarst to the drowned endokarst network. In the
707 surficial domain, the abundance of chalcedony filling the fracture network is compatible with
708 Group III silcrete pedogenesis of arid-alkaline environments as defined by Summerfield
709 (1983a, 1983b) and Wopfner (1983). In the endokarst, the alkaline tendency probably favored
710 silt-size quartz partial leaching. Periodical mixing with low acid rainwaters led to the growth
711 of drusy quartz in the residual intergranular space and to partial silicification of the
712 intrakarstic sediments (Nash and Ullyott, 2007; Ullyott and Nash, 2016).
713
714 *(iii) Stage 3: Early diagenetic ore deposition during the permanent evaporitic lake deposi-*
715 *tional system*
716 The karst reservoir was then subjected to two ore trapping stages during the
717 progressive emplacement by the permanent sulfate-rich lake system: a synsedimentary event
718 (Stage 3A) and an early burial process (Stage 3B) (Fig.15 – Stage 3).
719 *Stage 3A – Type I mineralization:* the karst sedimentary infilling was composed of
720 detrital-chemical depositional cycles compatible with humid-arid climate alternations and
721 emplacement of shallow sulfate-rich lake (Lopez and Mader, 1985). During humid periods,

part of the fine grained fraction derived from the weathering processes on the flanks of the paleo-highs was mobilized by the running waters and transported from exokarst systems toward the endokarstic cavities to form vadose silts and sands deposition. During the dry season, the lake depositional system was submitted to intense evaporation and evaporite precipitation. Part of the sulfate-rich waters and evaporite crystals were dragged toward the exokarst systems to give cyclic chemical laminae. At the same time, the presence of organic matter-rich material within karstic cavities favored the bacterial reduction of the downward percolating sulfates in the karst network. The source of metals probably derived from the meteoric leaching of outcropping previous MVT ore deposits from the paleoreliefs upstream the karst trap. Therefore, Type I mineralization clearly conjugated a synsedimentary gravity-driven mineralized brine with a BSR process that interacted in the meteoric karst network.

Stage 3B – Type II mineralization: during the early burial of the karst systems, the seal capacity of the Middle Triassic marls led to the trapping of the ascending hydrocarbon-rich fluids below this permeability barrier. Permanent downward sulfate-rich water still continued to percolate into the buried karst where permeable coarse material locally onlapped the paleosurface. The interaction between ascending hydrocarbon and the BSR zone formed a SMTZ which represented the upper chemical boundary for an underlying zone undersaturated in sulfates that led to the dissolution of previous buried Permian barite-rich ore deposits. Released barium, metals and sulfur were transported by the *per ascensum* reducing brine containing the hydrocarbon. During the ascension through the sedimentary pile, this solution reached the SMTZ window where dissolved sulfates were available. The increase of alkalinity was first responsible for the precipitation of ankerite on the walls of the cavities, closely associated with hydrocarbons markers. Barite and sulfides then precipitated, thus plugging the cavities to form the Type II mineralizations.

6. Conclusions

The originality of this work lies in the multi-scale analysis of an exceptional field example of continental diagenetic barite-sulfide deposits precipitated within meteoric karst systems. Ore deposits have been the subject of sedimentological and texture analysis, sulfur and strontium isotopes and fluid inclusions microthermometry. This methodology allows us to propose a genetic model of synsedimentary to early diagenetic metallogenesis in which we constrained all the factors whose interactions over time formed a favorable metallotect: karst dynamics, chemistry of the water table linked to climate and depositional environment changes, location of thermogenic hydrocarbons dysmigrations and the remobilization of former polymetallic deposits.

Four keypoints can be retained from this study:

- The importance of the interaction between the evolution of meteoric karsts during climate changes and the location of ore deposits. Epigene karstification plays both a fundamental precursor role, guiding the path of mineralizing fluids and constituting the main trap, and a passive role by undergoing the precipitation of the fluids which will then stop the karst evolution at the origin of mineralized paleokarsts.
- The predominant control of climate fluctuations, depositional environment changes and redox conditions at the water table on timing and texture of shallow continental diagenetic ore deposits. We show that the progressive transition from ephemeral playa lake to perennial evaporitic lake environments controls the supply of sulfates for mineralization and the position of the SMTZ by the interaction with ascending hydrocarbons.

- The significant impact of the thermogenic hydrocarbon migration in the metallogeny of sedimentary basins: passive role in the development of MVT ore deposits since the location of oil traps are constrained by the early mineralizations, and a foreground role in the supergene metallogeny by constituting a main vector in the redistribution of metals few meters below the SWI.
- The superimposition in a single trap of two very similar synsedimentary to early diagenetic mineralizations but implying different origins of fluids (surficial versus deep basinal brines) during the first step of burial along a karstic surface (notion of *"sliding metallogenic window effect"*).

780 **Acknowledgments**

781 We are grateful to Total Company (France) who funded all the field and laboratory
782 works during the thesis. We wish to thank Christophe Nevado and Doriane Delmas of
783 the Thin Section Lab at University of Montpellier for their work of high quality
784 which represented a solid foundation for this study. We also thank Bernard Boyer
785 and Claude Merlet at CNRS-University of Montpellier (France) for their technical
786 support with sulfur isotopes measurements on SIMS, and Olivier Bruguier for his
787 help in the strontium concentration analyses on LA-ICPMS at Géosciences Montpel-
788 lier. Finally, the Editor Sadoon Morad and the two reviewers are thanked for
789 thoughtful and constructive reviews which greatly improved the manuscript.

790 **Figures captions**

791

792 **Figure 1:** Geological setting of the Lodève Permian basin. A) Simplified geological map. The
793 black square indicates the location of the detailed geological map of the study area illustrated
794 in Fig.2A. B) North-south cross section of the Lodève half-graben. The location of the cross
795 section is indicated by the North-South bold line A-A' on Fig.1A.

796

797 **Figure 2:** A) Detailed geological map of the study area (see Fig.1A for the location). All the
798 studied outcrops are designated by a star and a letter, from a to j, that refers to the Appendix A.
799 B) SW-NE cross-section of the study area (the location is marked by a dashed line on Fig.2A).
800 C) Sedimentological log of the Triassic series above the post-rift unconformity of the Lodève
801 Basin.

802

803 **Figure 3:** The Roche Percée paleo-pothole. A) Geological map of the site. B) General
804 architecture of the paleokarst infill with the west side at left (View 1) and southern side at
805 right (View 2). C) Detailed views of the intrakarstic infilling with the section a (left) and
806 section b (right) located on the Fig.3A.

807

808 **Figure 4:** Close-up photos and photomicrographs of the Roche Percée paleo-pothole infill. A)
809 Successive breccia packages (c) bordered by the silicified calcschists (a) and including
810 collapsed silicified blocks (b) and gypsum-anhydrite boxworks (white arrows). B) Close-up
811 view of RP2 Facies showing millimetre-thick massive barite layers (white arrow) and nodules
812 (b) alternating with laminated dolomite-rich siltstone. C) Thin section of graded beds of the
813 RP2 Facies (plain-polarized light-PPL). D) Detailed view of a barite crystallite of the previous
814 thin section (C) showing clear corroded (yellow arrows) and broken surfaces (yellow circle)
815 (PPL). E. Photomicrograph of chalcopyrites crystallized within barite mineralization
816 (reflected light-RL).

817

818 **Figure 5**: General architecture of the Olmet Road paleo-lapiaz. A) Interpreted drawing of the
819 outcrop. B) Photo of the western part of the outcrop (see A for location) (tm: Triassic marls;
820 sd: sulfides-rich fine sandstones; ba: barite pockets; ib: sulfide impregnated bands and
821 fractures; cd: Cambrian dolomites. C) Photo of the central part of the outcrop (see A for

location) showing the main fault-damaged zone and barite-sulfide mineralizations in both hanging wall and footwall of the fault (cd: Cambrian dolomites; ba: barite; fb: tectonic breccia; ls: laminated sulfides-rich silty claystone; sd: sulfide-rich sandstone to siltstone; tm: Triassic marls).

Figure 6: Architecture and mineralized facies of the Montifort Road planar cavities string. A) General view and line-drawing of the outcrop showing the sub-planar endokarstic cavity cluster crossing the Cambrian calcschists. B) Close-up drawing of the southern part of the outcrop (see on A) with a detailed view of a planar cavity. C) Polished hand-sample section of a karstic cavity infill (ba: barite; gr: reverse graded granules; sic: silicification; black arrows: ankerite).

Figure 7: A) Photomicrographs of the base of figure 6C showing the intrakarstic sediments in the mineralized cavities of Montifort Road (an/white arrows: ankerite; gr: iron-rich silty dolomudstone grains; dq: drusy quartz; vs: geopetal silt infill) (Left PPL, Right cross-polarized light-XPL). B) Drusy ankerites growing on the phreatic drusy megaquartz (PPL). C) Contact zone between drusy ankerite and large barite slats (PPL). D) Photomicrograph in fluorescence X showing organic matter patches at the contact between drusy ankerite and host rock, and within barite mineralization. E) Scanning Electron Microscope (SEM) image illustrating numerous euhedral pyrites close to the contact between barite and late sparitic calcite.

Figure 8: General fabric of the Belbezet mine paleo-potholes and endokarst. A) Drawing of the main gallery close to the entrance showing the architecture of the ore deposit. B) Detail photo of the south-western face (see A for location) showing the Cambrian dolomites (cd) grooved by decimetre to meter-deep potholes (white dotted line) and filled by sulfide/barite-rich silty deposits (sb) reworked on top by bitumen-rich sulfide-barite deposits (rsb). C) Detail photo of bitumen-rich barite mineralization cementing a block of Cambrian dolomite (circled pencil is 15cm) (same legend than before). D) Close-up photo showing bitumen blebs (bi) and partly weathered grey copper sulfides (cs) cementing the white barite breccia.

Figure 9: Photomicrographs of primary fluid inclusions trapped within barite (PPL). A) Single-phase (1-phase FI) and two-phase (2-phase FI) inclusions in the barite (ba) sealing the endokarstic network of the Montifort Road outcrop. B) Essentially single-phase liquid inclusions (1-phase FI) entrapped within the barite of the Roche Percée paleo-pothole.

Figure 10: Histograms showing microthermometric Te, TmIce and Th data obtained for primary two-phase fluid inclusions entrapped within barite crystals of the Montifort Road outcrop corresponding to the mineralized infill of the planar cavities string (MR1 Facies) and barite precipitated within veins affected the Cambrian dolomites (MR2 Facies).

Figure 11: Synthetic paragenetic sequence and associated fabric for the post-rift Middle Triassic intrakarstic ore deposits.

Figure 12: Graph of $^{87}Sr/^{86}Sr$ vs Sr concentration (in ppm) of Middle Triassic post-rift barites belonging to the MR1, BM and RP2 Facies and the three distinct Late Permian syn-rift mineralizing events (described in Laurent et al., 2017). The range of strontium isotopic composition of the Triassic evaporites is reported from Koepnick et al. (1990) and Song et al. (2015). Analytical errors is ±0.000010 for $^{87}Sr/^{86}Sr$ in barites.

Figure 13: $\delta^{34}S$ diagram illustrating the signatures of the Triassic evaporites (grey star for gypsum and hexagon for anhydrite), barites (white circles) and chalcopyrites (black rectangle with error bars) of the Middle Triassic mineralizations (Type I and Type II) and Late Permian MVT ore deposits (Laurent et al., 2017). Analytical errors are ±0.2‰ for $\delta^{34}S$ in barites and Triassic evaporites, and ±1‰ for $\delta^{34}S$ in chalcopyrites.

Figure 14: $\delta^{34}S$-depth diagram showing the partitioning of barites and chalcopyrites for the Type I and Type II Middle Triassic ore deposits compared to the Triassic evaporites signature. The calculated $\varepsilon^{34}S$ (= $\delta^{34}S_{barite}$ - $\delta^{34}S_{chalcopyrite}$) is also indicated for each fronts (left figure). The mineralized front migrated upward during the progressive onlap and base level rise along the karstified paleosurface as a sliding biochemical window (right figure).

Figure 15: Conceptual model of the synsedimentary to early diagenetic ore deposition following the post-rift exhumation of the Lodève Basin's northern margin: Stage 1 – Exhumation, intense weathering and epigene karstification with vadose sediment infill; Stage 2 – Initial alkaline playa lake development, quartz leaching and vadose-phreatic silicifications during an increase of acidification; and Stage 3 – Perennial sulfate-rich lake development and synsedimentary to early diagenetic barite-sulfide trapping (Type I and Type II mineralizations).

Table 1: Fluid inclusion petrography and microthermomety data (Te, TmIce, Th and salinity) for the barites of the Middle Triassic ore deposits.

Table 2: $^{87}Sr/^{86}Sr$ and strontium concentration for barites and $\delta^{34}S$ for barites and synchronous chalcopyrites in the ore facies of the different studied area in this paper and for the three Late Permian MVT ore events presented in Laurent et al. (2017). Analytical errors are ±0.2‰ for $\delta^{34}S$ in barites and Triassic evaporites, ±1‰ for $\delta^{34}S$ in chalcopyrites and ±0.000010 for $^{87}Sr/^{86}Sr$ in barites.

Appendix A: Location and ore characteristics (architecture, mineralogy and classification) of the 10 sites studied in this entire wotk. Only 4 sites (in bold letters) have been chosen for a detailed description in this paper: Montifort Road, Roche Percée, Belbezet Mine and Olmet Road. The small letters refer to the map in Fig.2A.

907 **Bibliography**

908

909 Aloisi, G., Pierre, C., Rouchy, J.-M., Foucher, J.-P., Woodside, J., others, 2000. Methane-
910 related authigenic carbonates of eastern Mediterranean Sea mud volcanoes and their
911 possible relation to gas hydrate destabilisation. Earth Planet. Sci. Lett. 184, 321–338.

912 Aloisi, G., Wallmann, K., Bollwerk, S.M., Derkachev, A., Bohrmann, G., Suess, E., 2004.
913 The effect of dissolved barium on biogeochemical processes at cold seeps. Geochim.
914 Cosmochim. Acta 68, 1735–1748.

915 Alonso-Zarza, A. M. (2003). Palaeoenvironmental significance of palustrine carbonates and
916 calcretes in the geological record. Earth-Science Reviews, 60(3-4), 261-298.

917 Alperin, M. J., Reeburgh, W. S., Whiticar, M. J., 1988. Carbon and hydrogen isotope
918 fractionation resulting from anaerobic methane oxidation. *Global biogeochemical cycles*,
919 *2*(3), 279-288.

920 Aquilina, L., Dia, A.N., Boulègue, J., Bourgois, J., Fouillac, A.M., 1997. Massive barite
921 deposits in the convergent margin off Peru: Implications for fluid circulation within
922 subduction zones. Geochim. Cosmochim. Acta 61, 1233–1245.

923 Arndt, S., Brumsack, H.-J., Wirtz, K.W., 2006. Cretaceous black shales as active bioreactors:
924 a biogeochemical model for the deep biosphere encountered during ODP Leg 207
925 (Demerara Rise). Geochim. Cosmochim. Acta 70, 408–425.

926 Arning, E.T., Gaucher, E.C., van Berk, W., Schulz, H.-M., 2015. Hydrogeochemical models
927 locating sulfate-methane transition zone in marine sediments overlying black shales: A
928 new tool to locate biogenic methane? Mar. Pet. Geol. 59, 563–574.

929 Barnes, R.O., Goldberg, E.D., 1976. Methane production and consumption in anoxic marine
930 sediments. Geology 4, 297–300.

931 Bodnar, R.., 1994. Synthetic fluid inclusions: XII. The system H_2O-NaCl. Experimental
932 determination of the halite liquidus and isochores for a 40 wt% NaCl solution. Geochim.
933 Cosmochim. Acta 58, 1053–1063. https://doi.org/10.1016/0016-7037(94)90571-1

934 Bodnar, R.J., 1993. Revised equation and table for determining the freezing point depression
935 of H_2O-NaCl solutions. Geochim. Cosmochim. Acta; (United States) 57.

936 Bodnar, R.J., 1985. Fluid inclusion systematics in epithermal systems. Rev. Econ. Geol. 2,
937 73–97.

938 Borisenko, A.S., 1977. Study of the salt composition of solutions in gas-liquid inclusions in
939 minerals by the cryometric method. Sov. Geol. Geophys. 18, 11-18.

940 Borowski, W.S., Rodriguez, N.M., Paull, C.K., Ussler, W., 2013. Are ^{34}S-enriched authigenic
941 sulfide minerals a proxy for elevated methane flux and gas hydrates in the geologic
942 record? Mar. Pet. Geol. 43, 381–395. https://doi.org/10.1016/j.marpetgeo.2012.12.009

943 Borowski, W.S., Paull, C.K., Ussler, W., 1999. Global and local variations of interstitial
944 sulfate gradients in deep-water, continental margin sediments: Sensitivity to underlying
945 methane and gas hydrates. Mar. Geol. 159, 131–154.

946 Borowski, W.S., Paull, C.K., Ussler, W., 1997. Carbon cycling within the upper
947 methanogenic zone of continental rise sediments; an example from the methane-rich
948 sediments overlying the Blake Ridge gas hydrate deposits. Mar. Chem. 57, 299–311.

949 Bréhéret, J.-G., Brumsack, H.-J., 2000. Barite concretions as evidence of pauses in
950 sedimentation in the Marnes Bleues Formation of the Vocontian Basin (SE France).
951 Sediment. Geol. 130, 205–228.

952 Brown, P.E., 1989. FLINCOR; a microcomputer program for the reduction and investigation
953 of fluid-inclusion data. Am. Mineral. 74, 1390–1393.

954 Brown, P.E., Lamb, W.M., 1989. P-V-T properties of fluids in the system H_2O±CO_2±NaCl:
955 New graphical presentations and implications for fluid inclusion studies. Geochim.
956 Cosmochim. Acta 53, 1209–1221.

957 Brumsack, H.J., 1986. The inorganic geochemistry of Cretaceous black shales (DSDP Leg 41)
958 in comparison to modern upwelling sediments from the Gulf of California. Geol. Soc.
959 London, Spec. Publ. 21, 447–462.

960 Canfield, D.E., 2001. Biogeochemistry of sulfur isotopes. Rev. Mineral. Geochemistry 43,
961 607–636.

962 Cohen, A. I., Gordon, L., 1961. Co-precipitation in some binary sulphate systems. *Talanta*,
963 *7*(3-4), 195-211.

964 Crawford, M.L., 1981. Phase equilibria in aqueous fluid inclusions. Short course fluid
965 inclusions. Appl. Petrol 6, 75-100.

966 Dickens, G.R., 2001. Sulfate profiles and barium fronts in sediment on the Blake Ridge:
967 present and past methane fluxes through a large gas hydrate reservoir. Geochim.
968 Cosmochim. Acta 65, 529–543.

969 Duan, Z., Møller, N., Weare, J.H., 1992. An equation of state for the CH_4-CO_2-H_2O system: I.
970 Pure systems from 0 to 1000°C and 0 to 8000 bar. Geochim. Cosmochim. Acta 56,
971 2605–2617. https://doi.org/10.1016/0016-7037(92)90347-L

972 Echtler, H., Malavieille, J., 1990. Extensional tectonics, basement uplift and Stephano-
973 Permian collapse basin in a late Variscan metamorphic core complex (Montagne Noire,
974 Southern Massif Central). Tectonophysics 177, 125–138. https://doi.org/10.1016/0040-
975 1951 (90)90277-F

976 Fernandes, N.A., Gleeson, S.A., Magnall, J.M., Creaser, R.A., Martel, E., Fischer, B.J., Sharp,
977 R., 2017. The origin of Late Devonian (Frasnian) stratiform and stratabound mudstone-
978 hosted barite in the Selwyn Basin, Northwest Territories, Canada. Mar. Pet. Geol. 85, 1–
979 15. https://doi.org/10.1016/j.marpetgeo.2017.04.006

980 Freytet, P., & Plaziat, J. C., 1982. Continental carbonate sedimentation and pedogenesis-Late
981 Cretaceous and Early Tertiary of southern France. Contributions to Sedimentary Geology,
982 12, 213p.

983 Freytet, P., Plaziat, J.C., 1979. Les ooides calcaires continentaux: Diversité des formes, des
984 gisements, des modes de formation. Rech. Géographiques Astrasbg. 12, 69–80.

985 Gand, G., Lapeyrie, J., Garric, J., Nel, A., Schneider, J., Walter, H., 1997. Découverte
986 d'arthropodes et de bivalves inédits dans le Permien continental (Lodévois, France).
987 Comptes Rendus l'Académie des Sci. IIA-Earth Planet. Sci. 325, 891–898.

988 Goldberg, E.D., Arrhenius, G.O.S., 1958. Chemistry of Pacific pelagic sediments. Geochim.
989 Cosmochim. Acta 13, 153–212.

990 Goldstein, R.H., Reynolds, T.J., 1994. Systematics of fluid inclusions in diagenetic minerals,
991 SEPM short course ; SEPM, Tulsa, Okla.

992 Gordon, L., Reimer, C. C., Burtt, B. P., 1954. Distribution of strontium within barium sulfate
993 precipitated from homogeneous solution. Analytical Chemistry, 26(5), 842-846.

994 Günther, D., Heinrich, C.A., 1999. Enhanced sensitivity in laser ablation-ICP mass
995 spectrometry using helium-argon mixtures as aerosol carrier. J. Anal. At. Spectrom. 14,
996 1363–1368.

997 Harrison, A.G., Thode, H.G., 1958. Mechanism of the bacterial reduction of sulphate from
998 isotope fractionation studies. Trans. Faraday Soc. 54, 84–92.

999 Hay, R.L., Wiggins, B., 1980. Pellets, ooids, sepiolite and silica in three calcretes of the
1000 southwestern United States. Sedimentology 27, 559–576.

1001 Hoehler, T. M., Alperin, M. J., Albert, D. B., Martens, C. S., 1994. Field and laboratory
1002 studies of methane oxidation in an anoxic marine sediment: Evidence for a
1003 methanogen-sulfate reducer consortium. *Global Biogeochemical Cycles, 8*(4), 451-463.

1004 Hu, C.Y., Frank Yang, T., Burr, G.S., Chuang, P.C., Chen, H.W., Walia, M., Chen, N.C.,
1005 Huang, Y.C., Lin, S., Wang, Y., Chung, S.H., Huang, C. Da, Chen, C.H., 2017.
1006 Biogeochemical cycles at the sulfate-methane transition zone (SMTZ) and geochemical
1007 characteristics of the pore fluids offshore southwestern Taiwan. J. Asian Earth Sci. 149,
1008 172–183. https://doi.org/10.1016/j.jseaes.2017.07.002

1009 Jørgensen, B.B., Böttcher, M.E., Lüschen, H., Neretin, L.N., Volkov, I.I., 2004. Anaerobic
1010 methane oxidation and a deep H_2S sink generate isotopically heavy sulfides in Black Sea
1011 sediments. Geochim. Cosmochim. Acta 68, 2095–2118.

1012 Kastner, M., Elderfield, H., Martin, J.B., Suess, E., Kvenvolden, K.A., Garrison, R.E., 1990.
1013 Diagenesis and interstitial-water chemistry at the Peruvian continental margin—major
1014 constituents and strontium isotopes, in: Suess, E., von Huene, R., et Al., Proc. ODP, Sci.
1015 Results, 413–440.

1016 Knittel, K., Boetius, A., 2009. Anaerobic oxidation of methane: progress with an unknown
1017 process. Annu. Rev. Microbiol. 63, 311–334.

1018 Koepnick, R.B., Denison, R.E., Burke, W.H., Hetherington, E.A., Dahl, D.A., 1990.
1019 Construction of the Triassic and Jurassic portion of the Phanerozoic curve of seawater
1020 87Sr/86Sr. Chem. Geol. Isot. Geosci. Sect. 80, 327–349.

1021 Laurent, D., 2015. Marqueurs de la dynamique des fluides associée à l'enfouissement des
1022 bassins sédimentaires : Exemples du Bassin Permien de Lodève (France) et du North
1023 Viking Graben (Mer du Nord). Doctoral dissertation, Université de Montpellier, 622p.

1024 Laurent, D., Lopez, M., Chauvet, A., Sauvage, A.C., Buatier, M., Spangenberg, J.E., 2017.
1025 Sedimentary fluids/fault interaction during syn-rift burial of the Lodève Permian Basin
1026 (Hérault, France): An example of seismic-valve mechanism in active extensional faults.
1027 Mar. Pet. Geol. 88, 303–328. https://doi.org/10.1016/j.marpetgeo.2017.08.021

1028 Leach, D.L., Taylor, R.D., Fey, D.L., Diehl, S.F., Saltus, R.W., 2010. A deposit model for
1029 Mississippi Valley-Type lead-zinc ores. Miner. Depos. Model. Resour. Assess.

1030 Lerouge, C., Grangeon, S., Gaucher, E.C., Tournassat, C., Agrinier, P., Guerrot, C., Widory,
1031 D., Fléhoc, C., Wille, G., Ramboz, C., Vinsot, A., Buschaert, S., 2011. Mineralogical
1032 and isotopic record of biotic and abiotic diagenesis of the Callovian-Oxfordian clayey
1033 formation of Bure (France). Geochim. Cosmochim. Acta 75, 2633–2663.
1034 https://doi.org/10.1016/j.gca.2011.02.025

1035 Lopez, M., 1993. The Lodève Permian Basin. Post-Conference fieldtrip, in: Geofluids'93.
1036 Torquay, 190p.

1037 Lopez, M., 1992. Dynamique du passage d'un appareil terrigène à une plate-forme carbonatée
1038 en domaine semi-aride le Trias de Lodève, sud de la France. Doctoral dissertation,
1039 Université des Sciences et Techniques du Languedoc, Montpellier.

1040 Lopez, M., Gand, G., Garric, J., Körner, F., Schneider, J., 2008. The playa environments of
1041 the Lodève Permian basin (Languedoc-France). J. Iber. Geol. 34, 29–56.

1042 Lopez, M., Mader, D., 1985. Gravelly and sandy braidplain evolving into floodplain and
1043 playa lake deposits and vice versa in the Buntsandstein-facies sediments and marine
1044 incursions in the Triassic of the Lodève region (Southern France). In *Aspects of Fluvial*
1045 *Sedimentation in the Lower Triassic Buntsandstein of Europe*. Springer, Berlin,
1046 Heidelberg, 509-518.

1047 Lopez, M., Mader, D., 1992. Palaeoecological and palaeoenvironmental evolution of Permian
1048 and Triassic fluvial basins in Europe, Buntsandstein and Keuper Facies. Gustav Fischer
1049 Verlag publisher.

1050 Lopez, M., Petit, J.P., 2003. Outcrop analogues for Carboniferous and Rotliegende Dutch
1051 Oilfiels in the Lodève Permian Basin, South of France. Fieldtrip Guid. inédit, Lab. Dyn.
1052 la Lithosphère, Montpellier II.

1053 Machel, H.G., Krouse, H.R., Sassen, R., 1995. Products and distinguishing criteria of
1054 bacterial and thermochemical sulfate reduction. Appl. geochemistry 10, 373–389.

1055 Machel, H.G., 2001. Bacterial and thermochemical sulfate reduction in diagenetic settings –
1056 old and new insights. Sediment. Geol. 140, 143-175.

1057 Magnall, J.M., Gleeson, S.A., Stern, R.A., Newton, R.J., Poulton, S.W., Paradis, S., 2016.
1058 Open system sulphate reduction in a diagenetic environment - Isotopic analysis of barite
1059 ($\delta^{34}S$ and $\delta^{18}O$) and pyrite ($\delta^{34}S$) from the Tom and Jason Late Devonian Zn-Pb-Ba
1060 deposits, Selwyn Basin, Canada. Geochim. Cosmochim. Acta 180, 146–163.
1061 https://doi.org/10.1016/j.gca.2016.02.015

1062 Matter, A., Peters, T., Ramseyer, K., 1987. $^{87}Sr/^{86}Sr$-Verhältnisse und Sr-Gehalte von
1063 Tiefengrundwässern, Mineralien sowie Gesteinen aus dem Kristallin und der Trias der
1064 Nordschweiz. Eclogae Geol. Helv. 80, 579–592.

1065 Mazzullo, S. J., Birdwell, B. A., 1989. Syngenetic formation of grainstones and pisolites from
1066 fenestral carbonates in peritidal settings. Journal of Sedimentary Research, 59(4), 605-
1067 611.

1068 Meister, P., Mckenzie, J.A., Vasconcelos, C., Bernasconi, S., Frank, M., Gutjahr, M., Schrag,
1069 D.P., 2007. Dolomite formation in the dynamic deep biosphere: results from the Peru
1070 Margin. Sedimentology 54, 1007–1032.

1071 Moore, T.S., Murray, R.W., Kurtz, A.C., Schrag, D.P., 2004. Anaerobic methane oxidation
1072 and the formation of dolomite. Earth Planet. Sci. Lett. 229, 141–154.

1073 Nash, D.J., Ullyott, J.S., 2007. Silcrete. Geochemical sediments and landscapes 95–148.

1074 Niemann, H., Duarte, J., Hensen, C., Omoregie, E., Magalhaes, V.H., Elvert, M., Pinheiro,
1075 L.M., Kopf, A., Boetius, A., 2006. Microbial methane turnover at mud volcanoes of the
1076 Gulf of Cadiz. Geochim. Cosmochim. Acta 70, 5336–5355.

1077 Odin, B., 1986. Les formations permiennes, Autunien supérieur à Thuringien, du “bassin” de
1078 Lodève (Hérault, France) stratigraphie, minéralogie, paléoenvironnements, corrélations.
1079 Doctoral dissertation, Université d'Aix-Marseille, p. 375.

1080 Ohmoto, H., 1990. Systematics of sulphur isotopes in recent marine sediments and ancient
1081 sediment-hosted base metal deposits. Stable Isot. fluid Process. Miner. 23, 70–120.

1082 Ohmoto, H., Lasaga, A.C., 1982. Kinetics of reactions between aqueous sulfates and sulfides
1083 in hydrothermal systems. Geochim. Cosmochim. Acta 46, 1727–1745.

1084 Pin, C., Bassin, C., 1992. Evaluation of a strontium-specific extraction chromatographic
1085 method for isotopic analysis in geological materials. Anal. Chim. Acta 269, 249–255.

1086 Plaziat, J. C., Freytet, P., 1978. Le pseudo-microkarst pédologique: un aspect particulier des
1087 paléo-pédogenèses développées sur les dépôts calcaires lacustres dans le Tertiaire du
1088 Languedoc. Comptes Rendues Academie Science Paris, 286, 1661-1664.

1089 Postgate, J.R., Schwartz, W., 1985. The Sulfate-Reducing Bacteria (2nd Edition). J. Basic
1090 Microbiol. 25, 202. https://doi.org/10.1002/jobm.3620250311

1091 Raiswell, R., Fisher, Q.J., 2004. Rates of carbonate cementation associated with sulphate
1092 reduction in DSDP/ODP sediments: implications for the formation of concretions. Chem.
1093 Geol. 211, 71–85.

1094 Reeburgh, W.S., 1983. Rates of biogeochemical processes in anoxic sediments. Annu. Rev.
1095 Earth Planet. Sci. 11, 269–298.

1096 Reeburgh, W.S., 1976. Methane consumption in Cariaco Trench waters and sediments. Earth
1097 Planet. Sci. Lett. 28, 337–344.

1098 Renault, J., Brower, E., 1971. X-ray line broadening in the barium sulfate-strontium sulfate
1099 series. American Mineralogist: Journal of Earth and Planetary Materials, 56(7-8), 1481-
1100 1485.

1101 Riedinger, N., Kasten, S., Gröger, J., Franke, C., Pfeifer, K., 2006. Active and buried
1102 authigenic barite fronts in sediments from the Eastern Cape Basin. Earth Planet. Sci. Lett.
1103 241, 876–887.

1104 Rodriguez, N.M., Paull, C.K., Borowski, W.S., 2000. Zonation of authigenic carbonates
1105 within gas hydrate-bearing sedimentary sections on the Blake Ridge: offshore

1106 southeastern north America 1, in: Proceedings of the Ocean Drilling Program. Scientific
1107 Results, 301–312.

1108 Roedder, E., 1984. Fluid inclusion. Rev. Mineral. 12, 1–394.

1109 Routhier, P., 1980. Où sont les métaux pour l'avenir?: les provinces métalliques: essai
1110 demétallogénie globale. Editions du BRGM.

1111 Rye, R. O., Ohmoto, H., 1974. Sulfur and carbon isotopes and ore genesis: a review.
1112 *Economic Geology*, *69*(6), 826-842.

1113 Snyder, G.T., Dickens, G.R., Castellini, D.G., 2007. Labile barite contents and dissolved
1114 barium concentrations on Blake Ridge: new perspectives on barium cycling above gas
1115 hydrate systems. J. Geochemical Explor. 95, 48–65.

1116 Song, H., Wignall, P.B., Tong, J., Song, H., Chen, J., Chu, D., Tian, L., Luo, M., Zong, K.,
1117 Chen, Y., Lai, X., Zhang, K., Wang, H., 2015. Integrated Sr isotope variations and global
1118 environmental changes through the Late Permian to early Late Triassic. Earth Planet. Sci.
1119 Lett. 424, 140–147. https://doi.org/10.1016/j.epsl.2015.05.035

1120 Spangenberg J.E., Lavrić J., Meisser N., Serneels V., 2010. Sulfur isotope analysis

1121 of cinnabar from Roman wall paintings by EA/IRMS –tracking the origin of

1122 archaeological red pigments and their authenticity. Rapid Communications in Mass

1123 Spectrometry, 24, 2812-2816.

1124 Sterner, S. M., Bodnar, R. J., 1984. Synthetic fluid inclusions in natural quartz I.
1125 Compositional types synthesized and applications to experimental geochemistry.
1126 *Geochimica et Cosmochimica Acta*, *48*(12), 2659-2668.

1127 Summerfield, M.A., 1983a. Petrography and diagenesis of silcrete from the Kalahari Basin
1128 and Cape coastal zone, Southern Africa. J. Sediment. Res. 53, 895–909.

1129 Summerfield, M.A., 1983b. Silcrete as a palaeoclimatic indicator: evidence from southern
1130 Africa. Palaeogeogr. Palaeoclimatol. Palaeoecol. 41, 65–79.

1131 Torres, M.E., Brumsack, H.J., Bohrmann, G., Emeis, K.C., 1996. Barite fronts in continental
1132 margin sediments: a new look at barium remobilization in the zone of sulfate reduction
1133 and formation of heavy barites in diagenetic fronts. Chem. Geol. 127, 125–139.

1134 Ullyott, J.S., Nash, D.J., 2016. Distinguishing pedogenic and non-pedogenic silcretes in the
1135 landscape and geological record. Proc. Geol. Assoc. 127, 311–319.

1136 Ulrich, M. R., Bodnar, R. J., 1988. Systematics of stretching of fluid inclusions; II, Barite at 1
1137 atm confining pressure. *Economic Geology, 83*(5), 1037-1046.

1138 Van Achterbergh, E., Ryan, C. G., Jackson, S. E., Griffin, W. L., Sylvester, P., 2001. Laser-
1139 Ablation-ICPMS in the Earth Sciences—Principles and Applications. Mineralogical
1140 Association of Canada Short Course Series, 40.

1141 Wibberley, C.A.J., Petit, J.-P., Rives, T., 2007. The effect of tilting on fault propagation and
1142 network development in sandstone-shale sequences: a case study from the Lodève Basin,
1143 southern France. J. Geol. Soc. London. 164, 599–608.

1144 Wopfner, H., 1983. Environment of silcrete formation: a comparison of examples from
1145 Australia and the Cologne Embayment, West Germany. Geol. Soc. London, Spec. Publ.
1146 11, 151–158.

1147 Wortmann, U.G., Bernasconi, S.M., Böttcher, M.E., 2001. Hypersulfidic deep biosphere
1148 indicates extreme sulfur isotope fractionation during single-step microbial sulfate
1149 reduction. Geology 29, 647–650.

1150 Zhou, X., Chen, D., Dong, S., Zhang, Y., Guo, Z., Wei, H., Yu, H., 2015. Diagenetic barite
1151 deposits in the Yurtus Formation in Tarim Basin, NW China: Implications for barium
1152 and sulfur cycling in the earliest Cambrian. Precambrian Res. 263, 79–87.
1153 https://doi.org/10.1016/j.precamres.2015.03.006.

1154

1155

A)

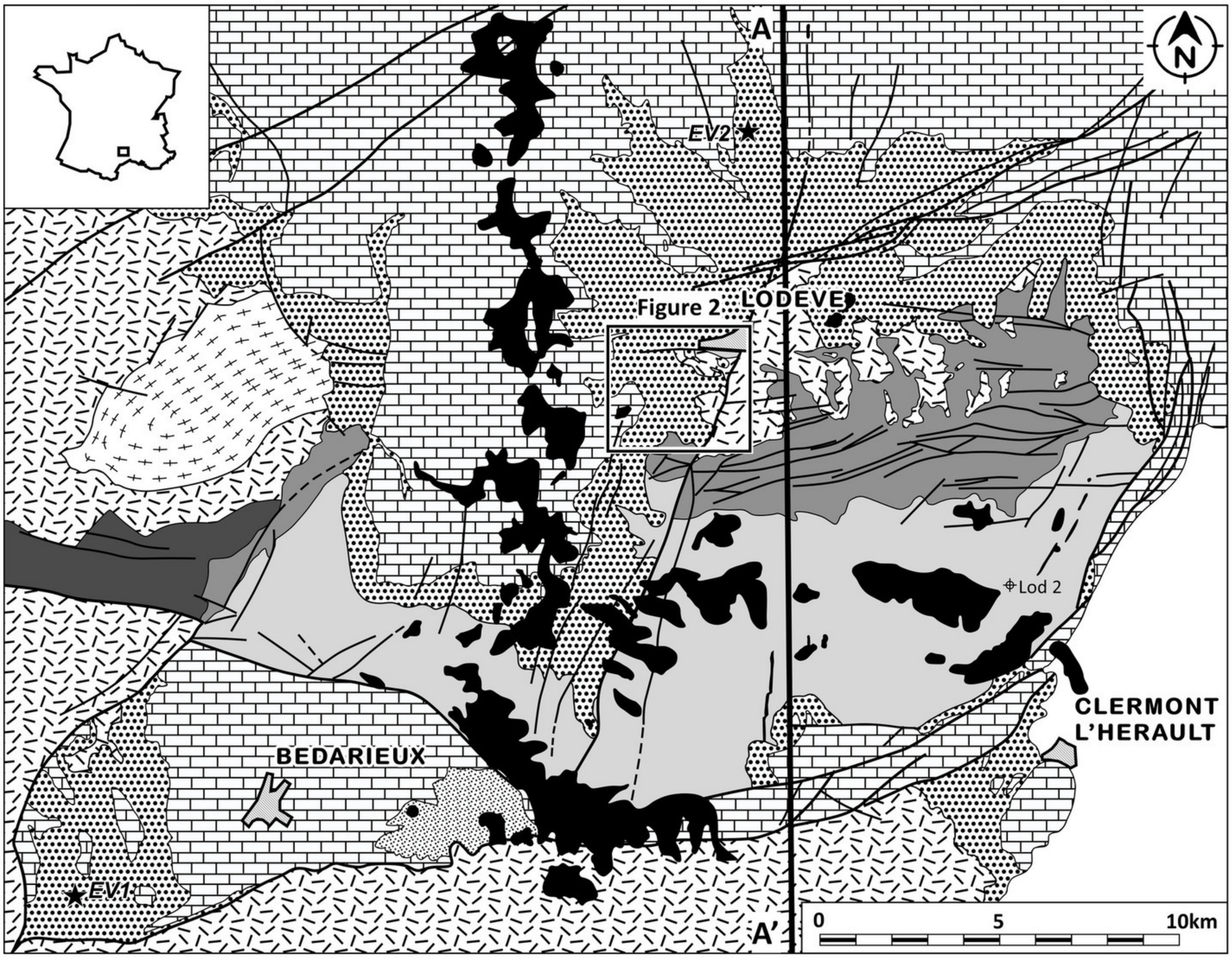
A
A'
N
EV2
Figure 2
LODEVE
Lod 2
CLERMONT
L'HERAULT
BEDARIEUX
EV1
0
5
10km

B)

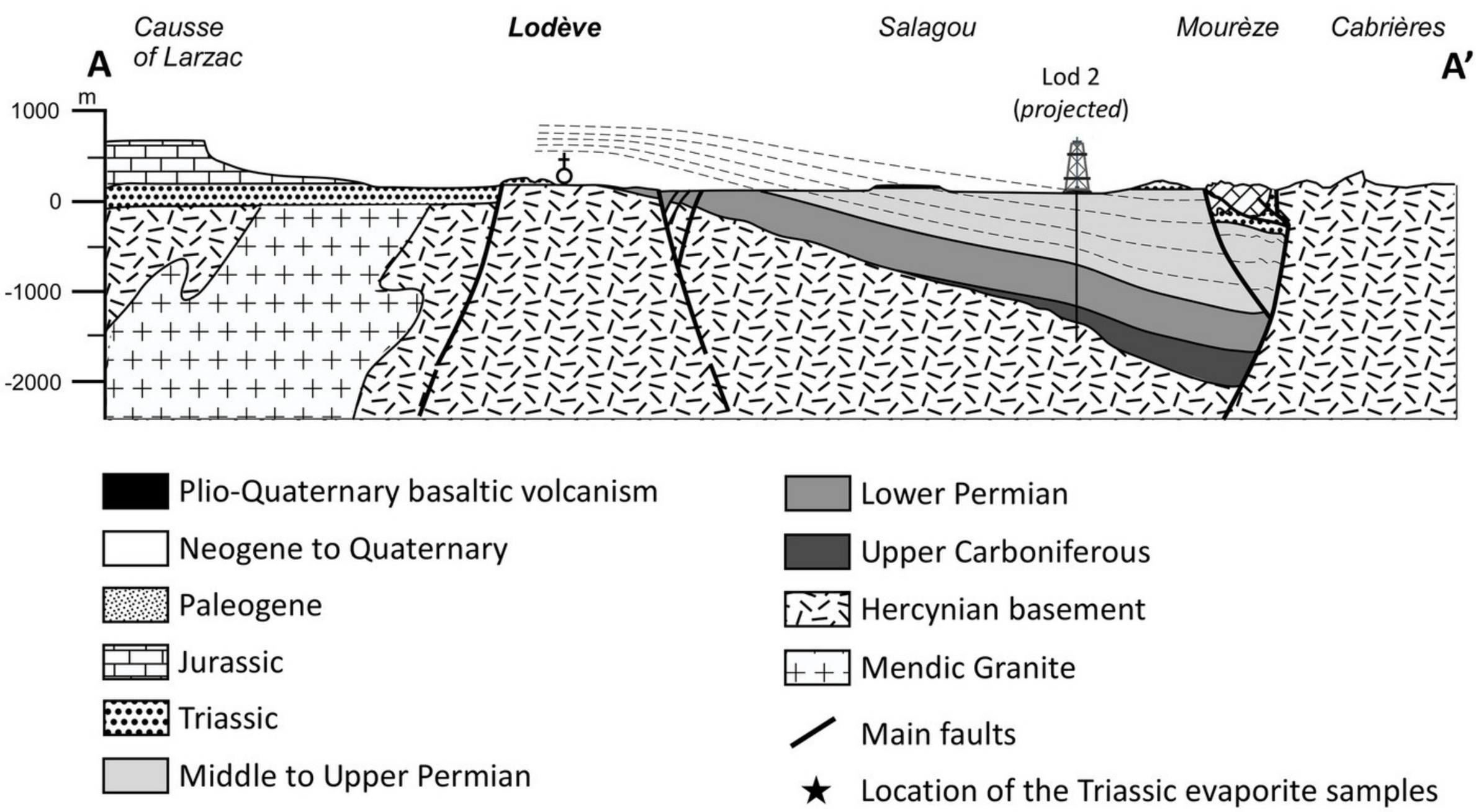
N
S
A
A'
Causse
of Larzac
Lodève
Salagou
Mourèze
Cabrières
Lod 2
(projected)
m
1000
0
-1000
-2000
Plio-Quaternary basaltic volcanism
Neogene to Quaternary
Paleogene
Jurassic
Triassic
Middle to Upper Permian
Lower Permian
Upper Carboniferous
Hercynian basement
Mendic Granite
Main faults
Location of the Triassic evaporite samples

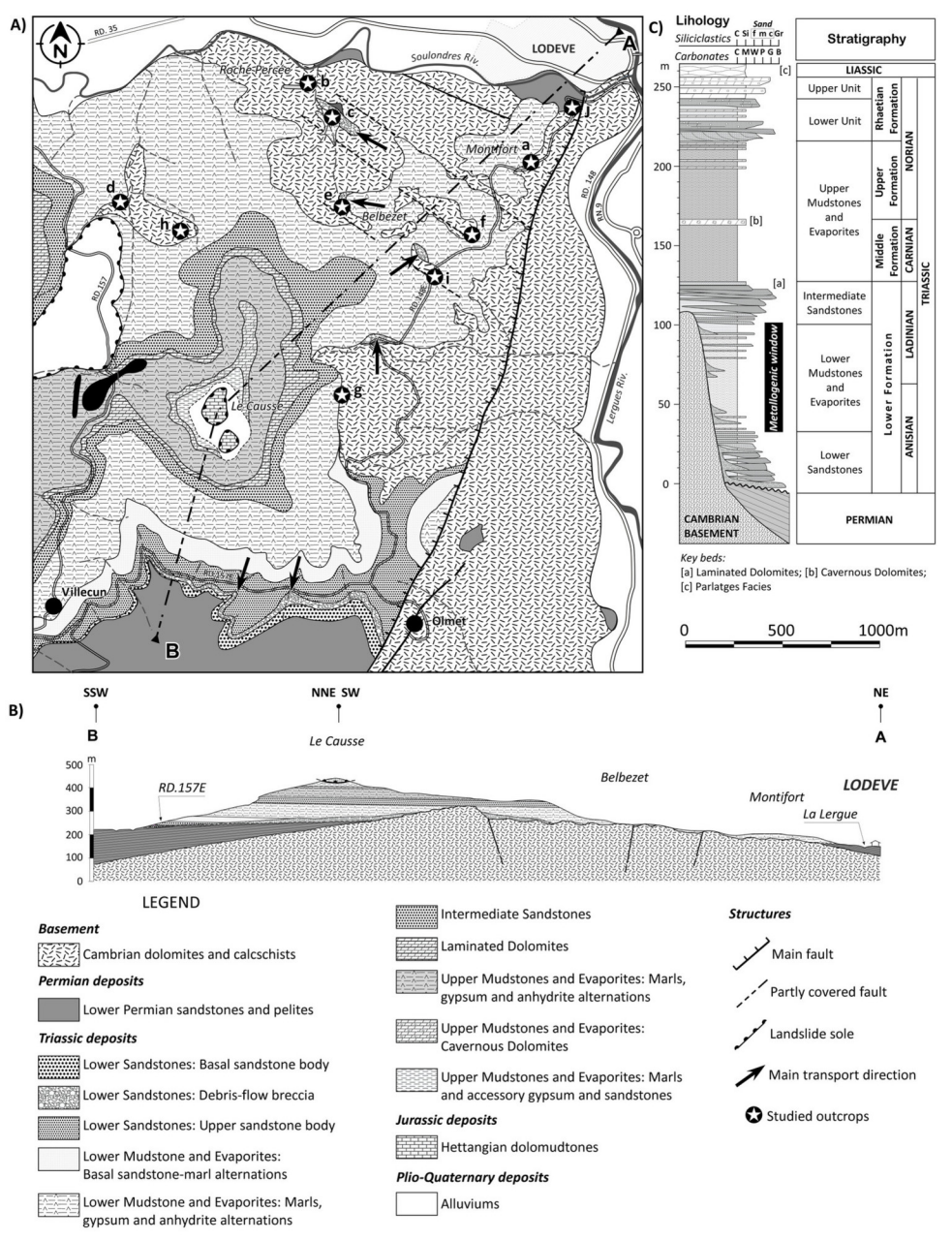
A)
N
RD. 35
Soulondres Riv.
LODEVE
A
Roche Percée
b
c
j
Montfort
a
RD. 148
RD.9
d
e
Belbezet
f
h
i
RD.157
RD.157E
Le Causse
g
Lergues Riv.
Villecun
B
Olmet
C)
Lihology
Siliciclastics
Carbonates
Sand
C Si f m cGr
C M W P G B
Stratigraphy
m
[c]
250
200
[b]
150
[a]
100
50
0
Metallogenic window
CAMBRIAN BASEMENT
LIASSIC
Upper Unit
Lower Unit
Rhaetian Formation
NORIAN
Upper Mudstones and Evaporites
Upper Formation
Middle Formation
CARNIAN
Intermediate Sandstones
Lower Mudstones and Evaporites
Lower Formation
LADINIAN
ANISIAN
TRIASSIC
Lower Sandstones
PERMIAN
Key beds:
[a] Laminated Dolomites; [b] Cavernous Dolomites;
[c] Parlatges Facies
0
500
1000m
B)
SSW
B
NNE SW
Le Causse
NE
A
500
400
300
200
100
0
m
RD.157E
Belbezet
Montfort
LODEVE
La Lergue
LEGEND
Basement
Cambrian dolomites and calcschists
Permian deposits
Lower Permian sandstones and pelites
Triassic deposits
Lower Sandstones: Basal sandstone body
Lower Sandstones: Debris-flow breccia
Lower Sandstones: Upper sandstone body
Lower Mudstone and Evaporites: Basal sandstone-marl alternations
Lower Mudstone and Evaporites: Marls, gypsum and anhydrite alternations
Intermediate Sandstones
Laminated Dolomites
Upper Mudstones and Evaporites: Marls, gypsum and anhydrite alternations
Upper Mudstones and Evaporites: Cavernous Dolomites
Upper Mudstones and Evaporites: Marls and accessory gypsum and sandstones
Jurassic deposits
Hettangian dolomudstones
Plio-Quaternary deposits
Alluviums
Structures
Main fault
Partly covered fault
Landslide sole
Main transport direction
Studied outcrops

A)

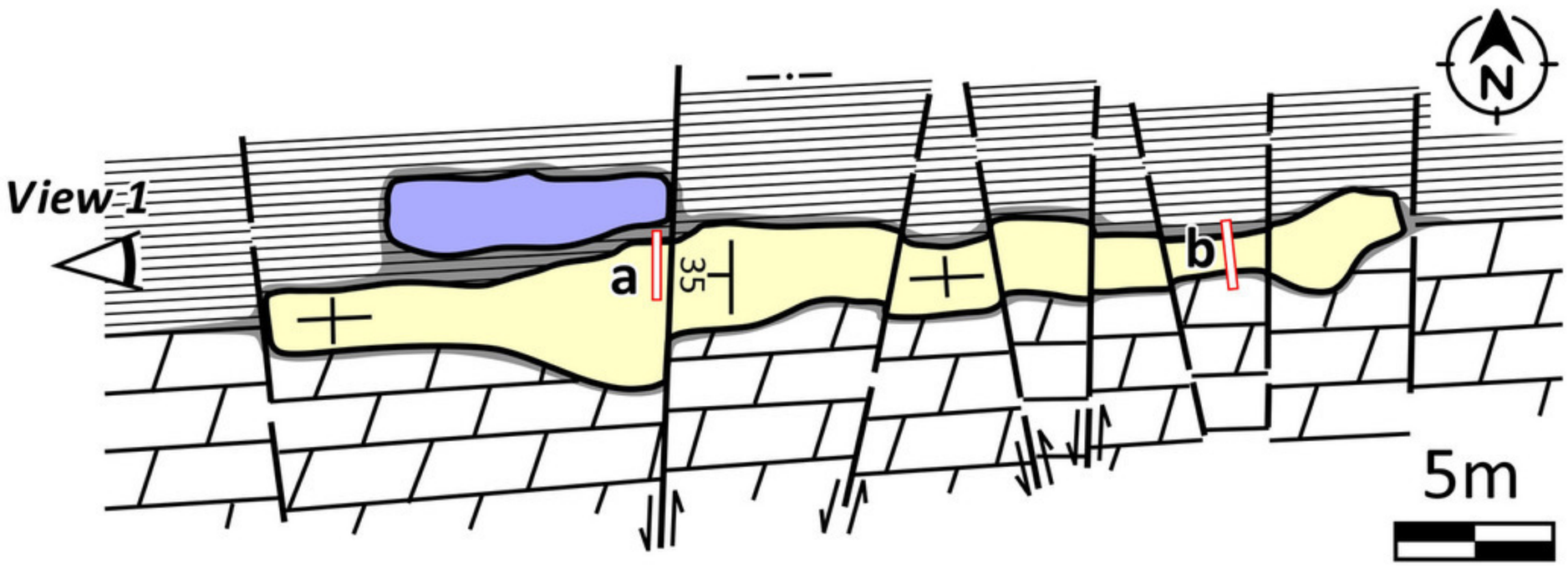

N S W E

View 2

B)

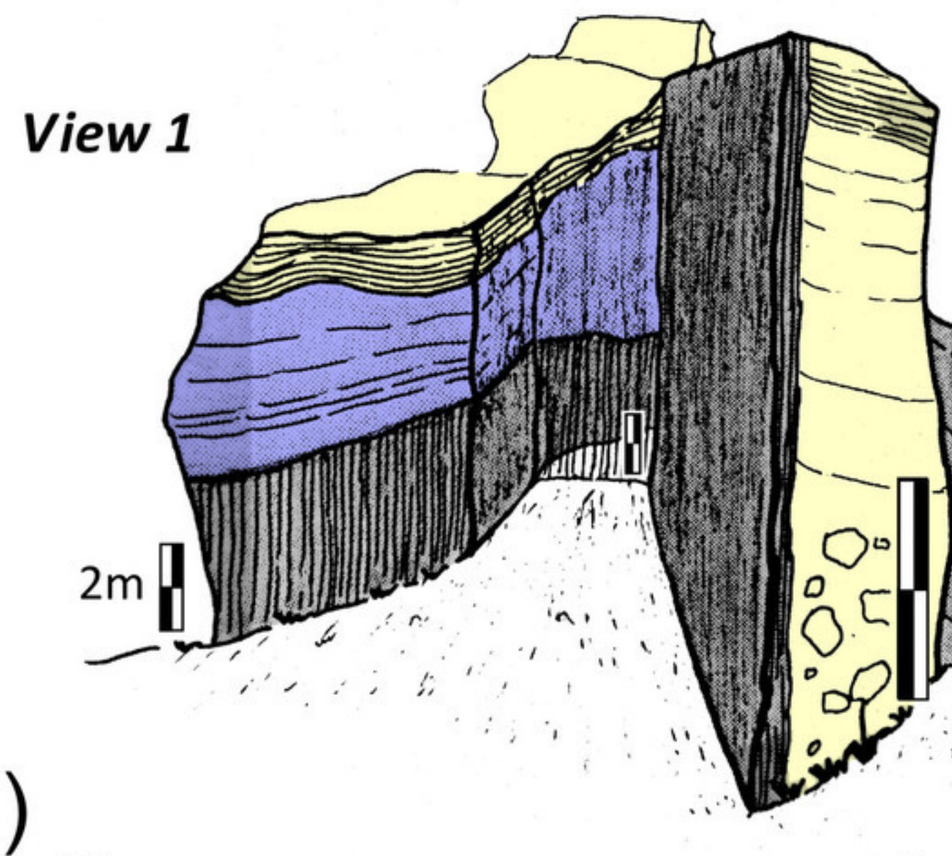

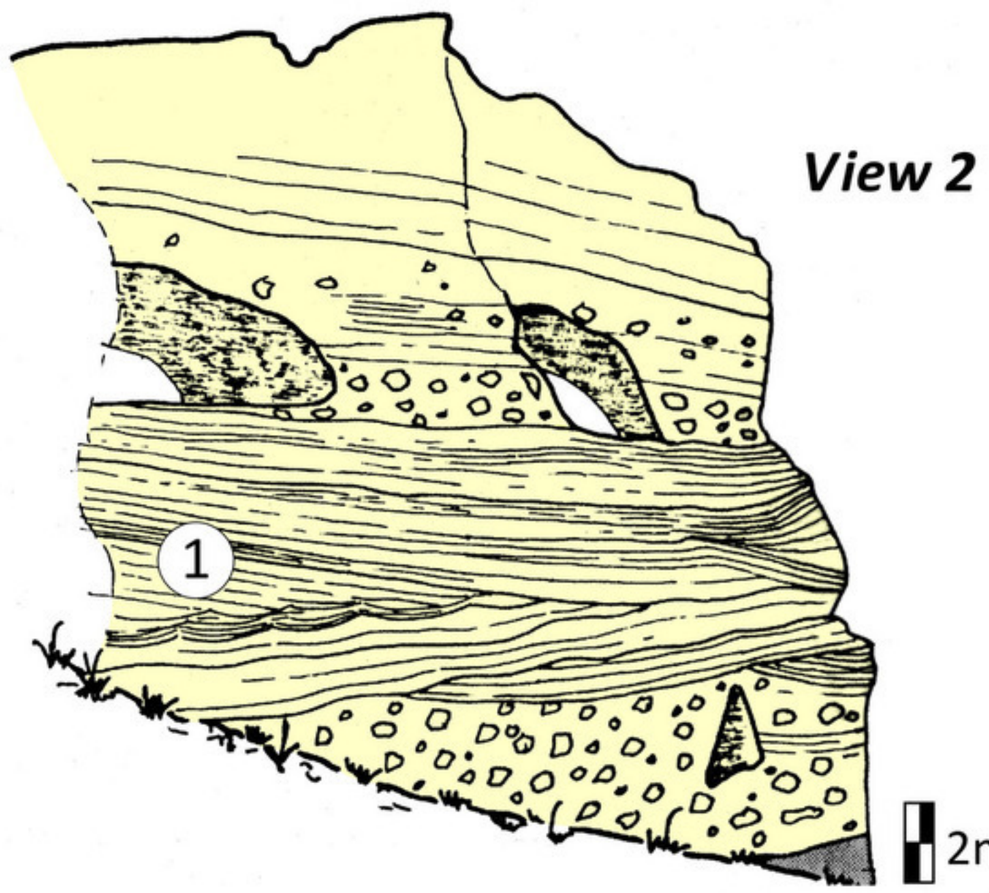

N S N S

C)

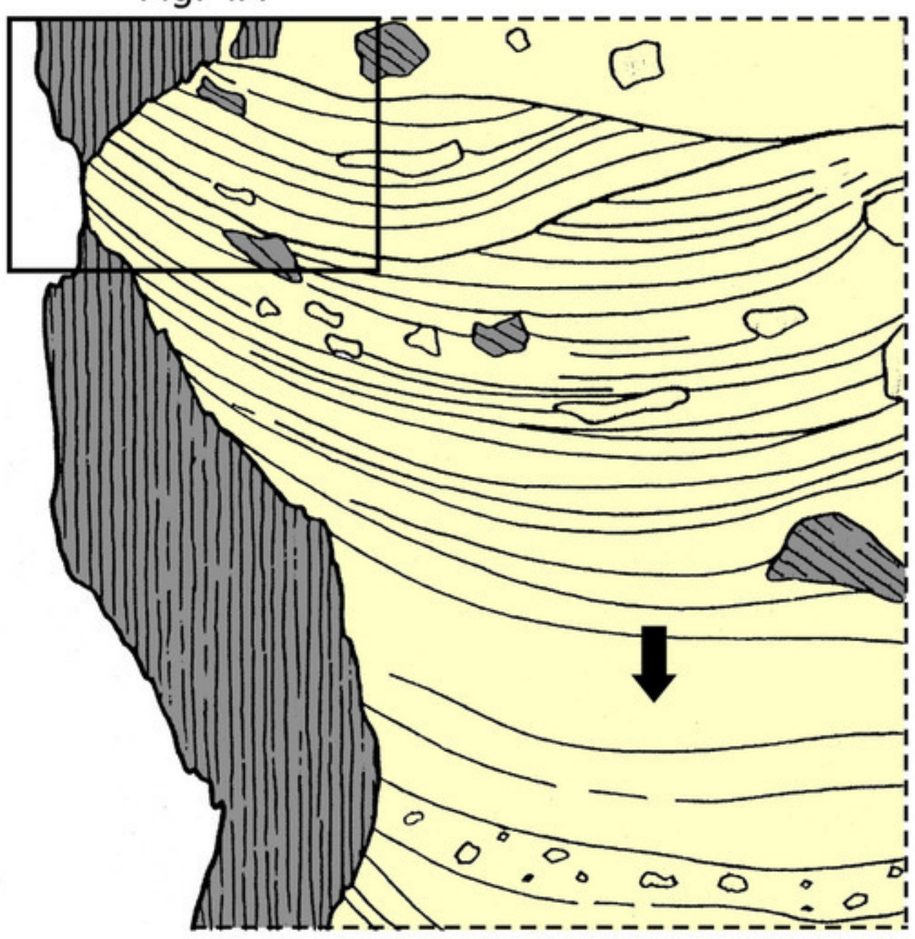

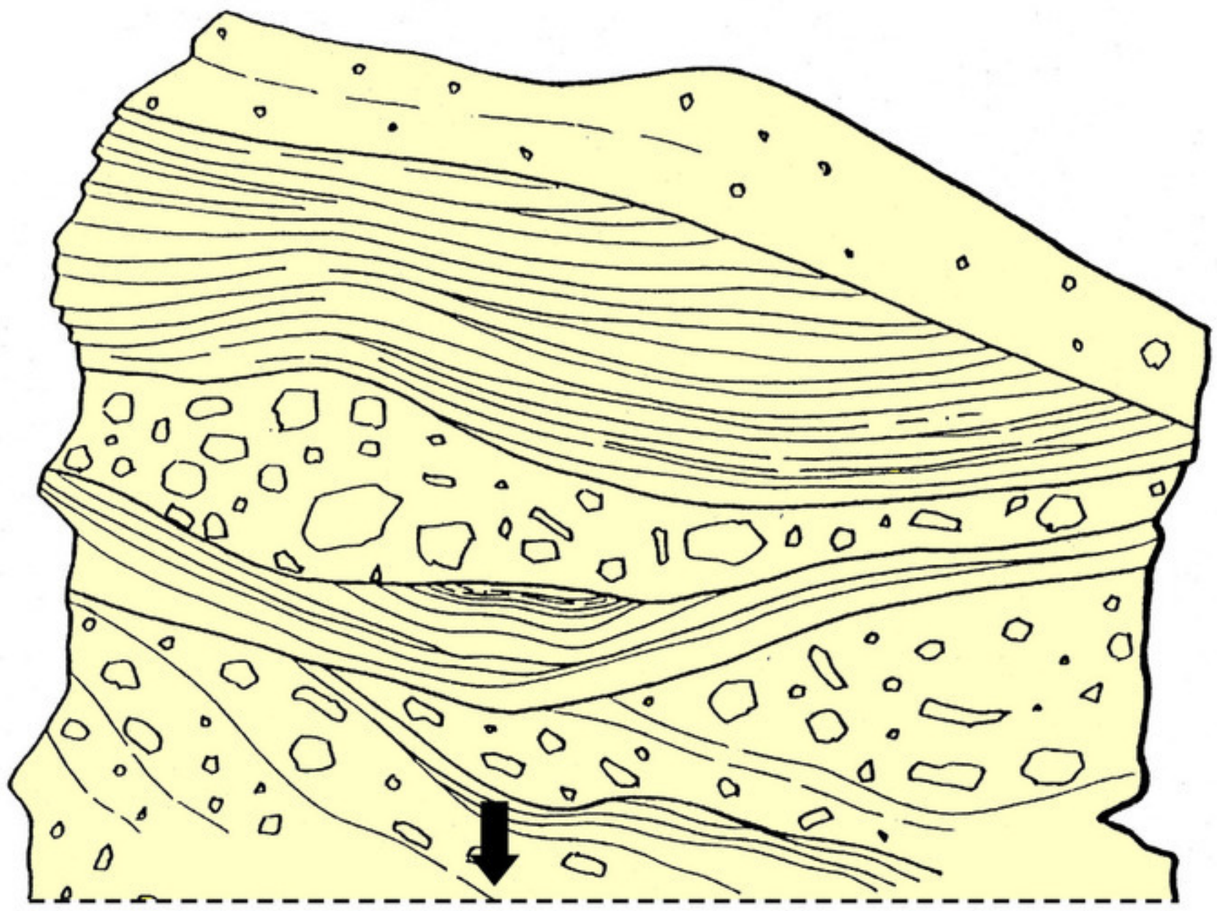

Section a 10 cm *Section* b 10 cm

1 Tepee antiform structures

Dolomite

Calcschists

Barite-silica rich intrakastic breccia (Facies RP3)

Barite-silica rich intrakarstic arenite (Facies RP2)

Fine organic-rich intrakastic sandstone (Facies RP1)

Silicified facies

Karstic withdrawal

strike-slip fault

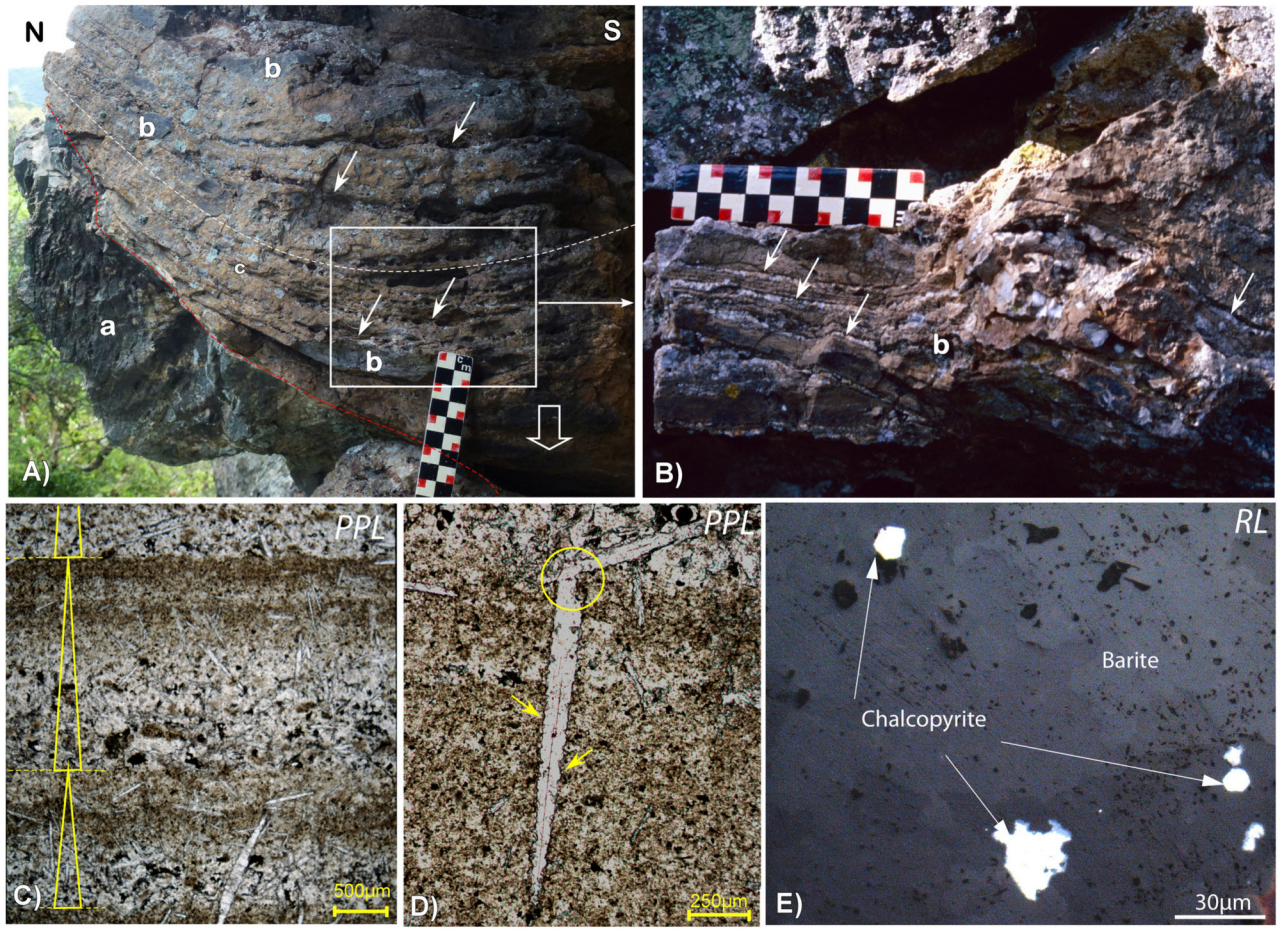
N
S
b
b
c
a
b
A)
b
B)
PPL
C)
500µm
PPL
D)
250µm
RL
Barite
Chalcopyrite
E)
30µm

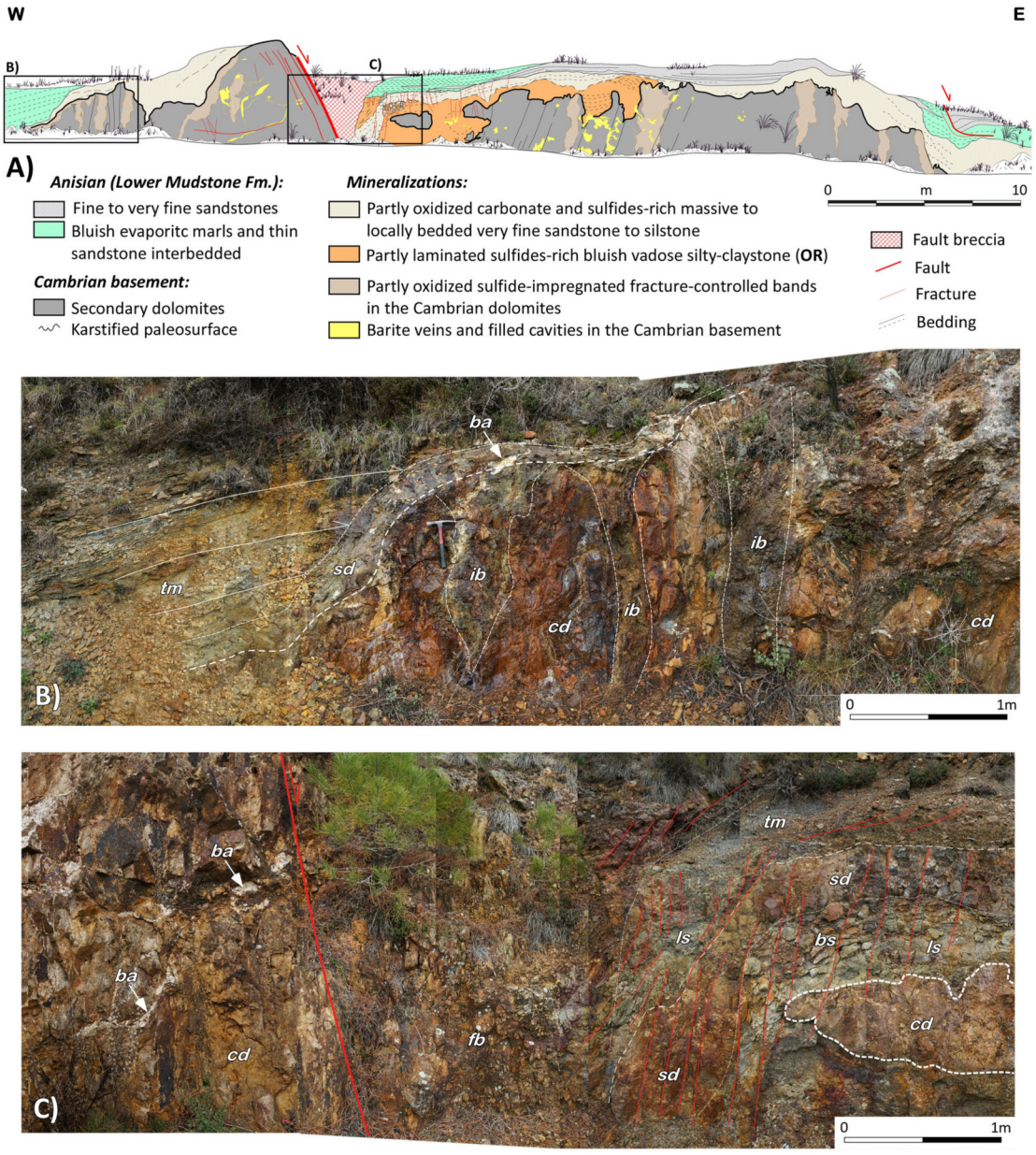
W
E
B)
C)
A)
Anisian (Lower Mudstone Fm.):
Fine to very fine sandstones
Bluish evaporitc marls and thin sandstone interbedded
Cambrian basement:
Secondary dolomites
Karstified paleosurface
Mineralizations:
Partly oxidized carbonate and sulfides-rich massive to locally bedded very fine sandstone to silstone
Partly laminated sulfides-rich bluish vadose silty-claystone (OR)
Partly oxidized sulfide-impregnated fracture-controlled bands in the Cambrian dolomites
Barite veins and filled cavities in the Cambrian basement
0 m 10
Fault breccia
Fault
Fracture
Bedding
ba
tm
sd
ib
cd
ib
ib
cd
B)
0 1m
ba
ba
cd
fb
tm
sd
ls
bs
ls
cd
sd
C)
0 1m

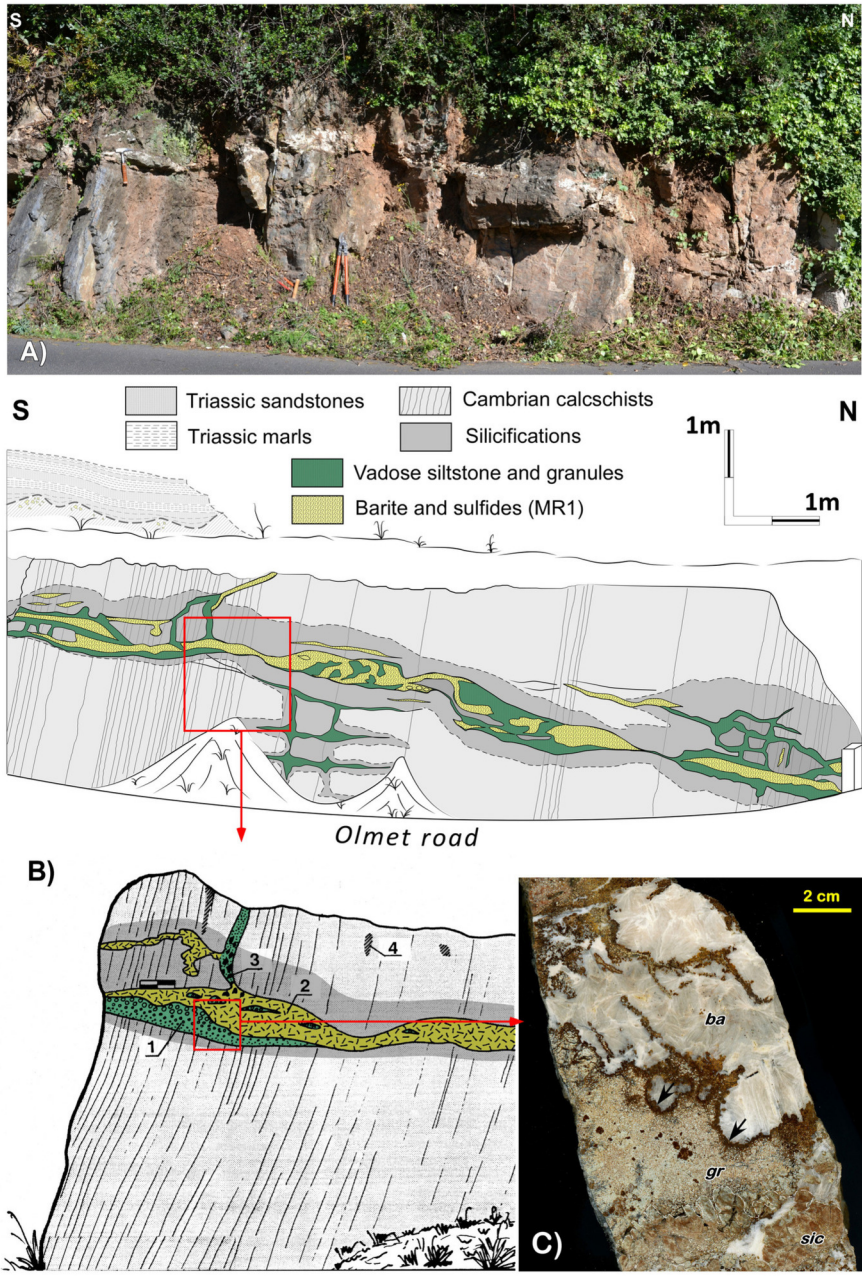
S
N
A)
S
N
Triassic sandstones
Triassic marls
Cambrian calcschists
Silicifications
Vadose siltstone and granules
Barite and sulfides (MR1)
1m
1m
Olmet road
B)
1
2
3
4
2 cm
ba
gr
sic
C)

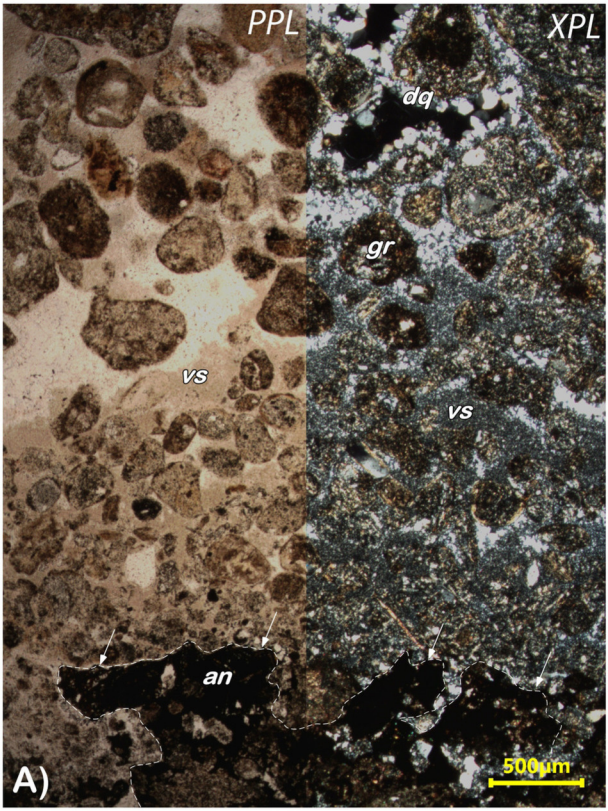
PPL
XPL
dq
gr
vs
vs
an
500µm
A)

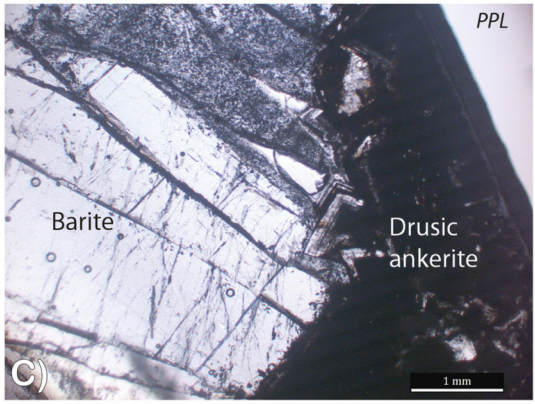
PPL
Barite
Drusic ankerite
1 mm
C)

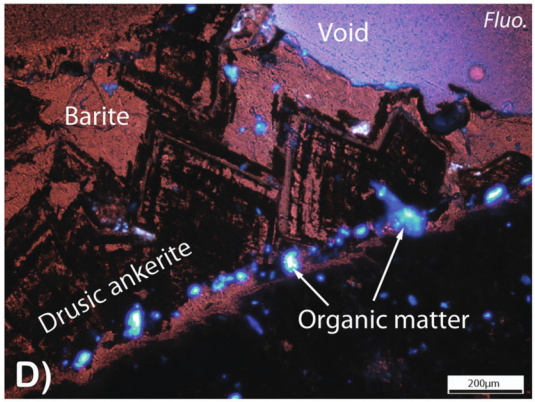
Fluo.
Void
Barite
Drusic ankerite
Organic matter
200µm
D)

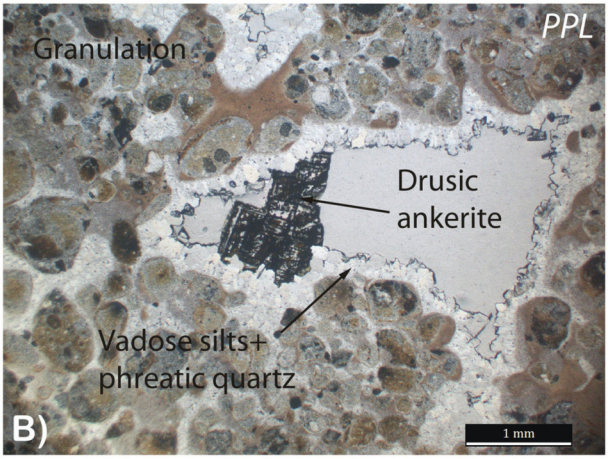
PPL
Granulation
Drusic ankerite
Vadose silts+ phreatic quartz
1 mm
B)

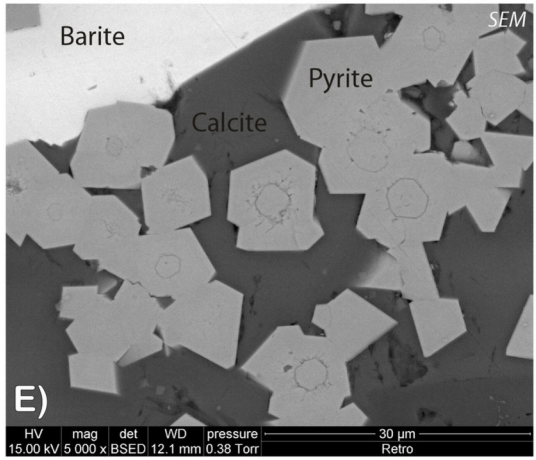
SEM
Barite
Pyrite
Calcite
E)
HV mag det WD pressure
15.00 kV 5 000 x BSED 12.1 mm 0.38 Torr
30 µm
Retro

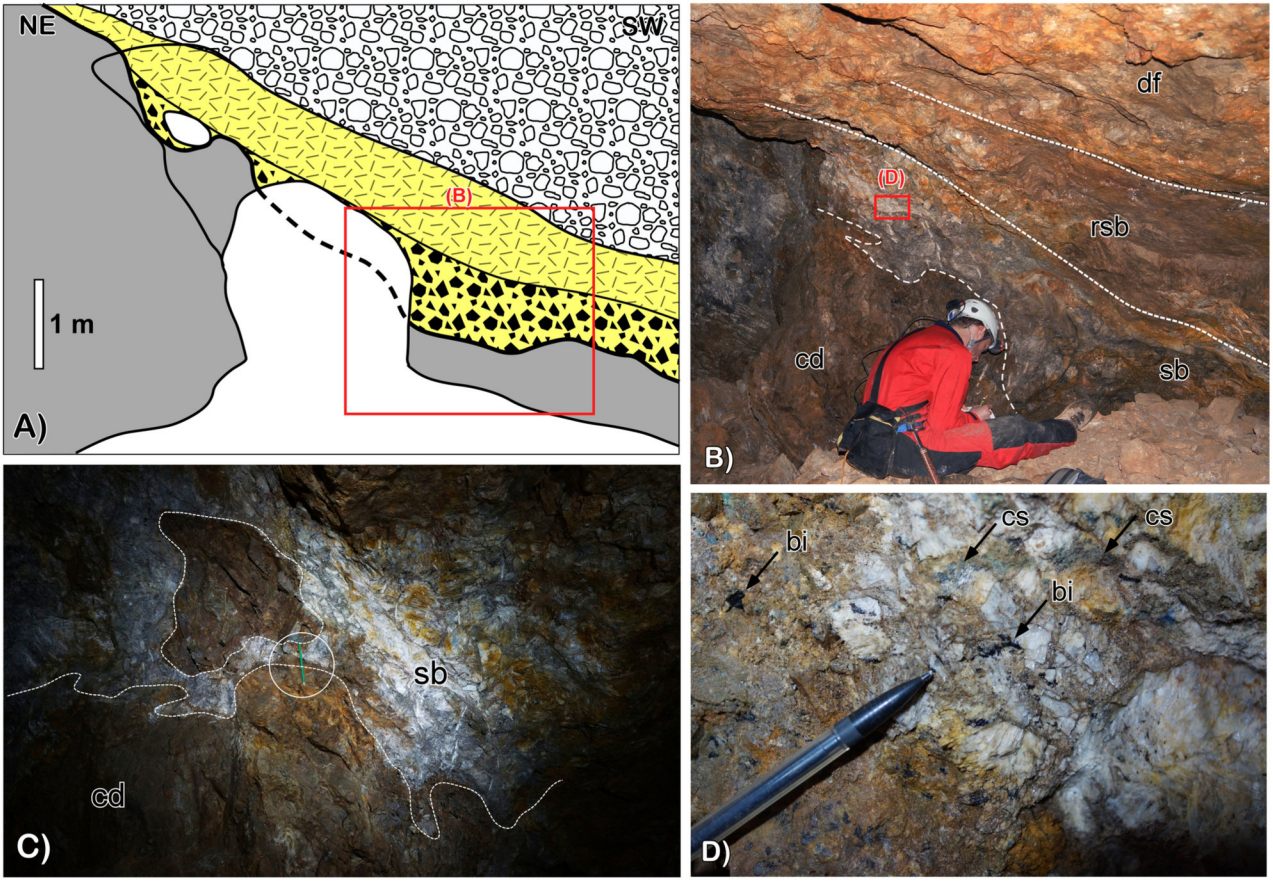
NE
SW
(B)
1 m
A)
df
(D)
rsb
cd
sb
B)
sb
cd
C)
cs
cs
bi
bi
D)
Matrix supported conglomerate (debris-flow deposit) Middle Triassic
Reworked bitumen-rich sulfide-barite deposit
Partly silicified Cambrian dolomites
Sulfide-barite-rich silty clayey intrakarstic deposit (**BM**)

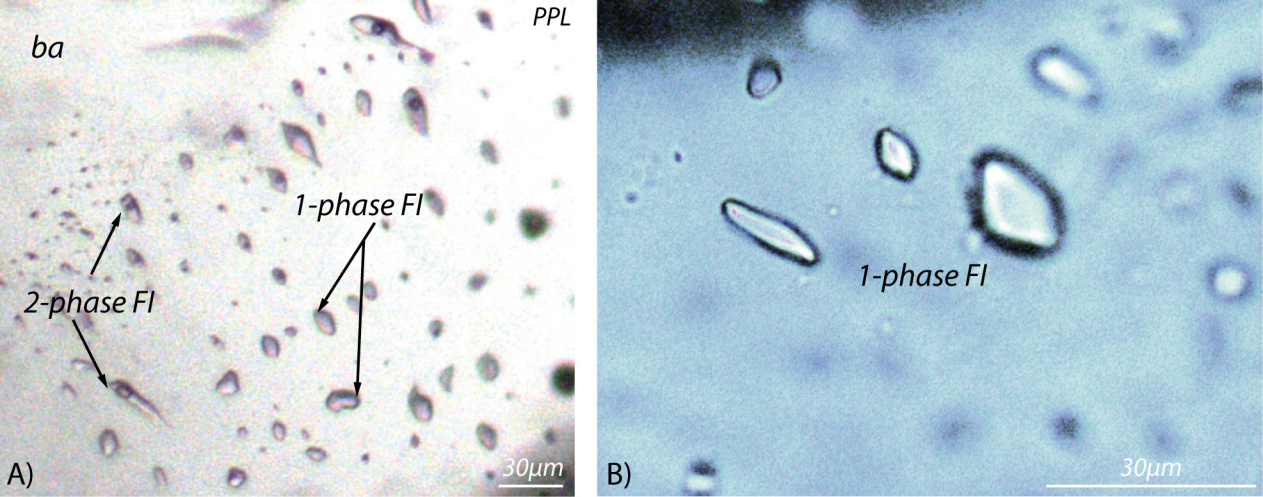
ba
PPL
1-phase FI
2-phase FI
A)
30µm
1-phase FI
B)
30µm

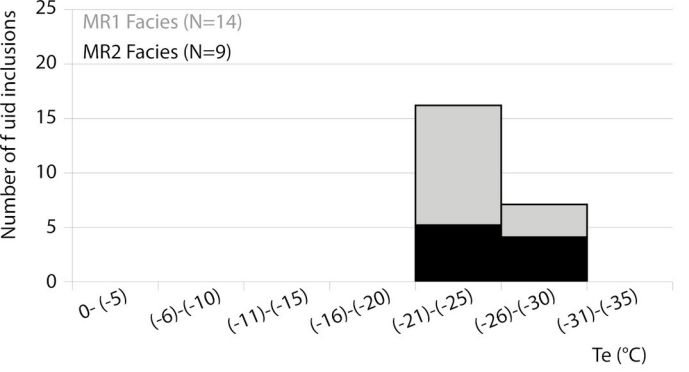
MR1 Facies (N=14)
MR2 Facies (N=9)
Number of fluid inclusions
0
5
10
15
20
25
0- (-5)
(-6)-(-10)
(-11)-(-15)
(-16)-(-20)
(-21)-(-25)
(-26)-(-30)
(-31)-(-35)
Te (°C)

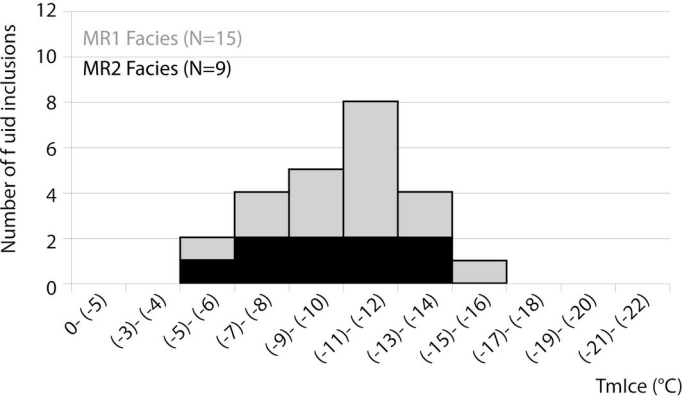
MR1 Facies (N=15)
MR2 Facies (N=9)
Number of fluid inclusions
0
2
4
6
8
10
12
0- (-5)
(-3)- (-4)
(-5)- (-6)
(-7)- (-8)
(-9)- (-10)
(-11)- (-12)
(-13)- (-14)
(-15)- (-16)
(-17)- (-18)
(-19)- (-20)
(-21)- (-22)
TmIce (°C)

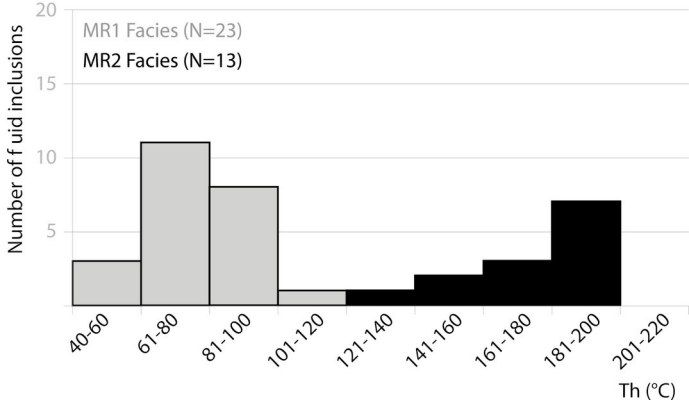
MR1 Facies (N=23)
MR2 Facies (N=13)
Number of fluid inclusions
5
10
15
20
40-60
61-80
81-100
101-120
121-140
141-160
161-180
181-200
201-220
Th (°C)

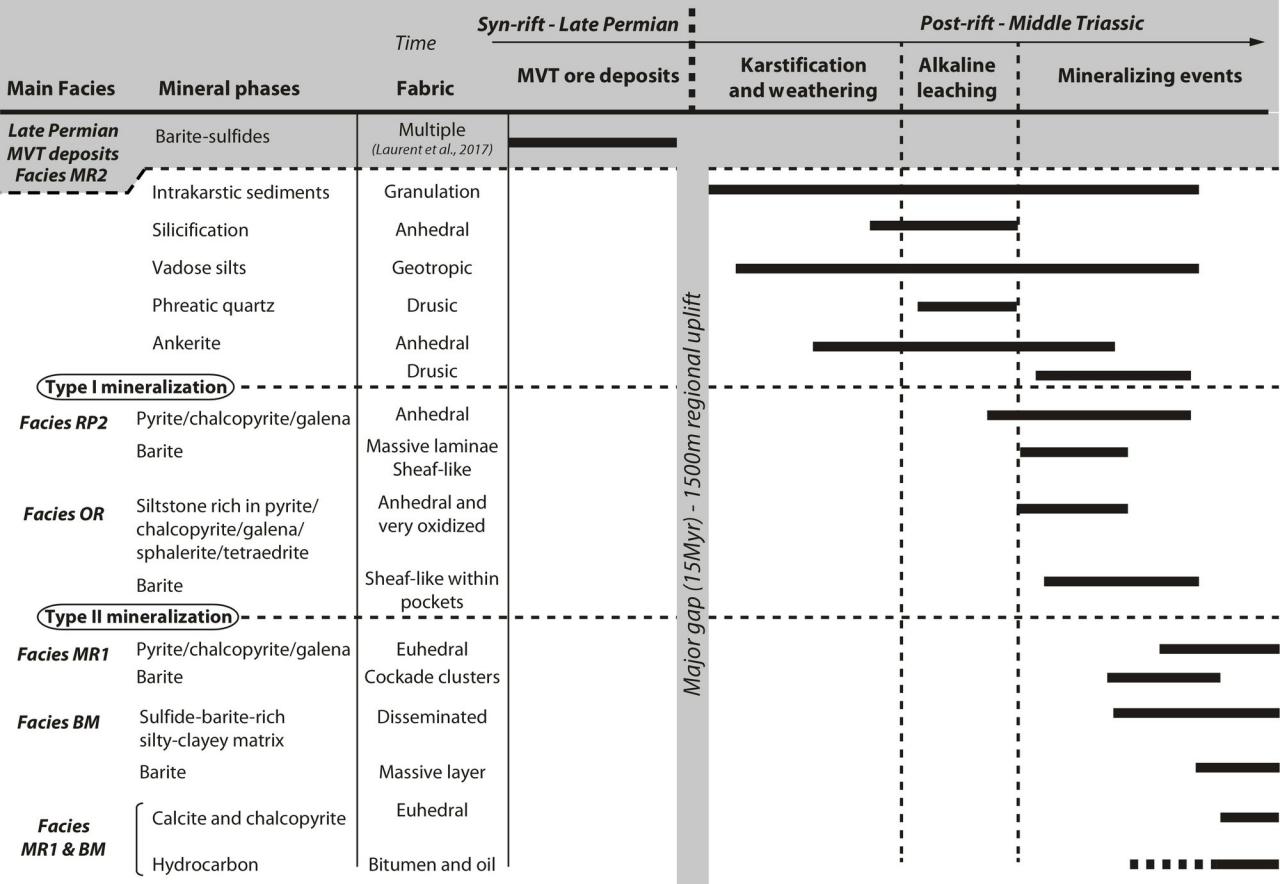
Time
Syn-rift - Late Permian
Post-rift - Middle Triassic
Main Facies
Mineral phases
Fabric
MVT ore deposits
Karstification and weathering
Alkaline leaching
Mineralizing events
Late Permian MVT deposits Facies MR2
Barite-sulfides
Multiple
(Laurent et al., 2017)
Intrakarstic sediments
Granulation
Silicification
Anhedral
Vadose silts
Geotropic
Phreatic quartz
Drusic
Ankerite
Anhedral
Drusic
Type I mineralization
Facies RP2
Pyrite/chalcopyrite/galena
Anhedral
Barite
Massive laminae
Sheaf-like
Facies OR
Siltstone rich in pyrite/ chalcopyrite/galena/ sphalerite/tetraedrite
Anhedral and very oxidized
Barite
Sheaf-like within pockets
Type II mineralization
Facies MR1
Pyrite/chalcopyrite/galena
Euhedral
Barite
Cockade clusters
Facies BM
Sulfide-barite-rich silty-clayey matrix
Disseminated
Barite
Massive layer
Facies MR1 & BM
Calcite and chalcopyrite
Euhedral
Hydrocarbon
Bitumen and oil
Major gap (15Myr) - 1500m regional uplift

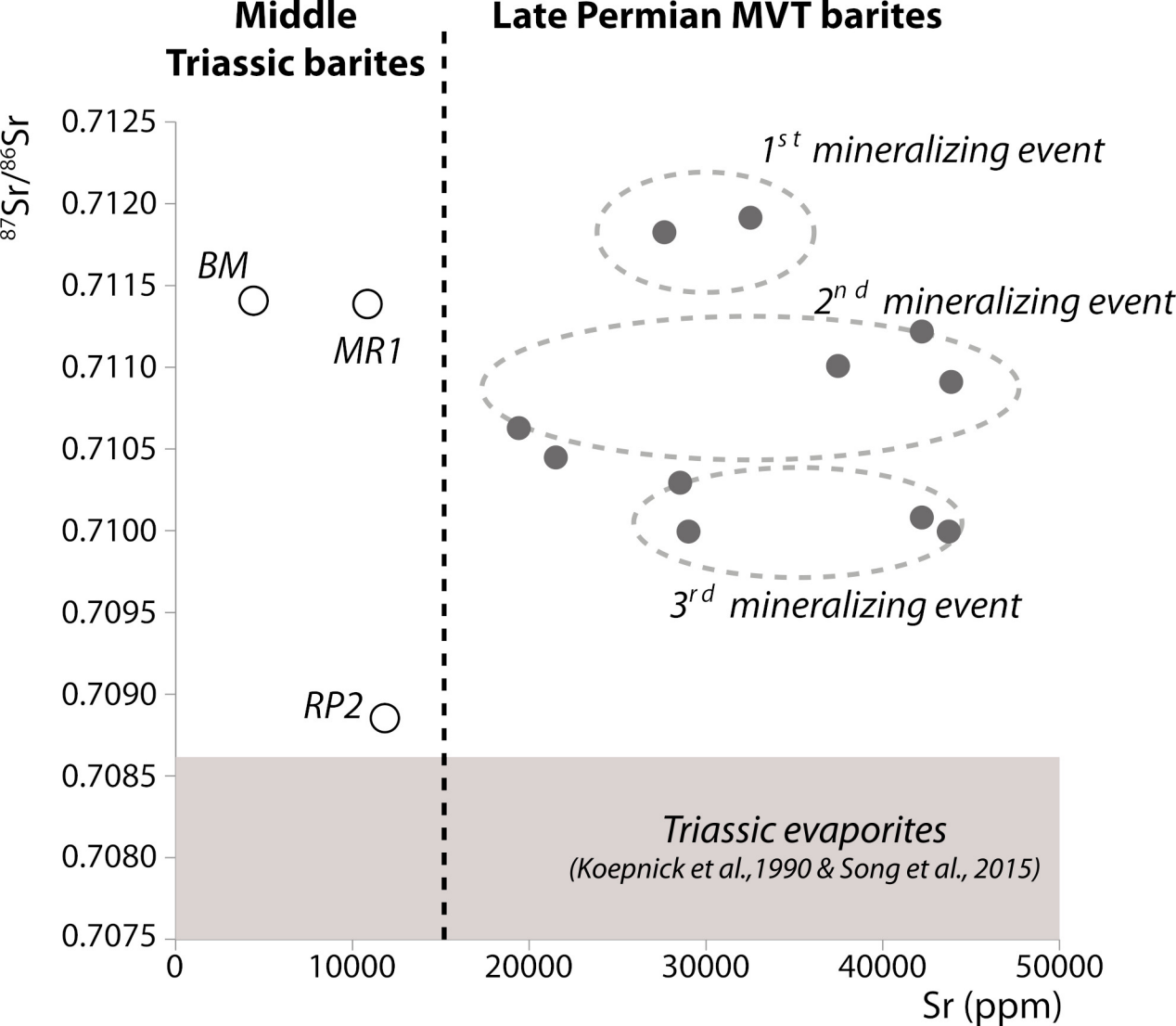
Middle Triassic barites
Late Permian MVT barites
$^{87}Sr/^{86}Sr$
0.7125
0.7120
0.7115
0.7110
0.7105
0.7100
0.7095
0.7090
0.7085
0.7080
0.7075
BM
MR1
RP2
1st mineralizing event
2nd mineralizing event
3rd mineralizing event
Triassic evaporites
(Koepnick et al.,1990 & Song et al., 2015)
0
10000
20000
30000
40000
50000
Sr (ppm)

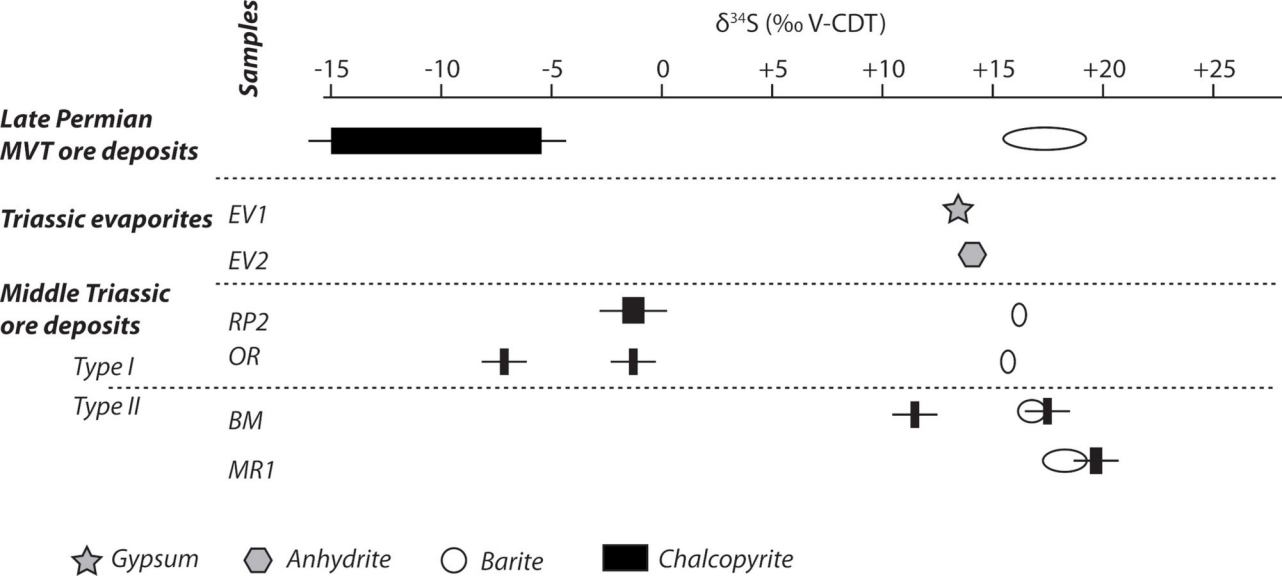
Samples
δ34S (‰ V-CDT)
-15
-10
-5
0
+5
+10
+15
+20
+25
Late Permian MVT ore deposits
Triassic evaporites
EV1
EV2
Middle Triassic ore deposits
RP2
0
Type I
OR
0
Type II
BM
MR1
Gypsum
Anhydrite
Barite
Chalcopyrite

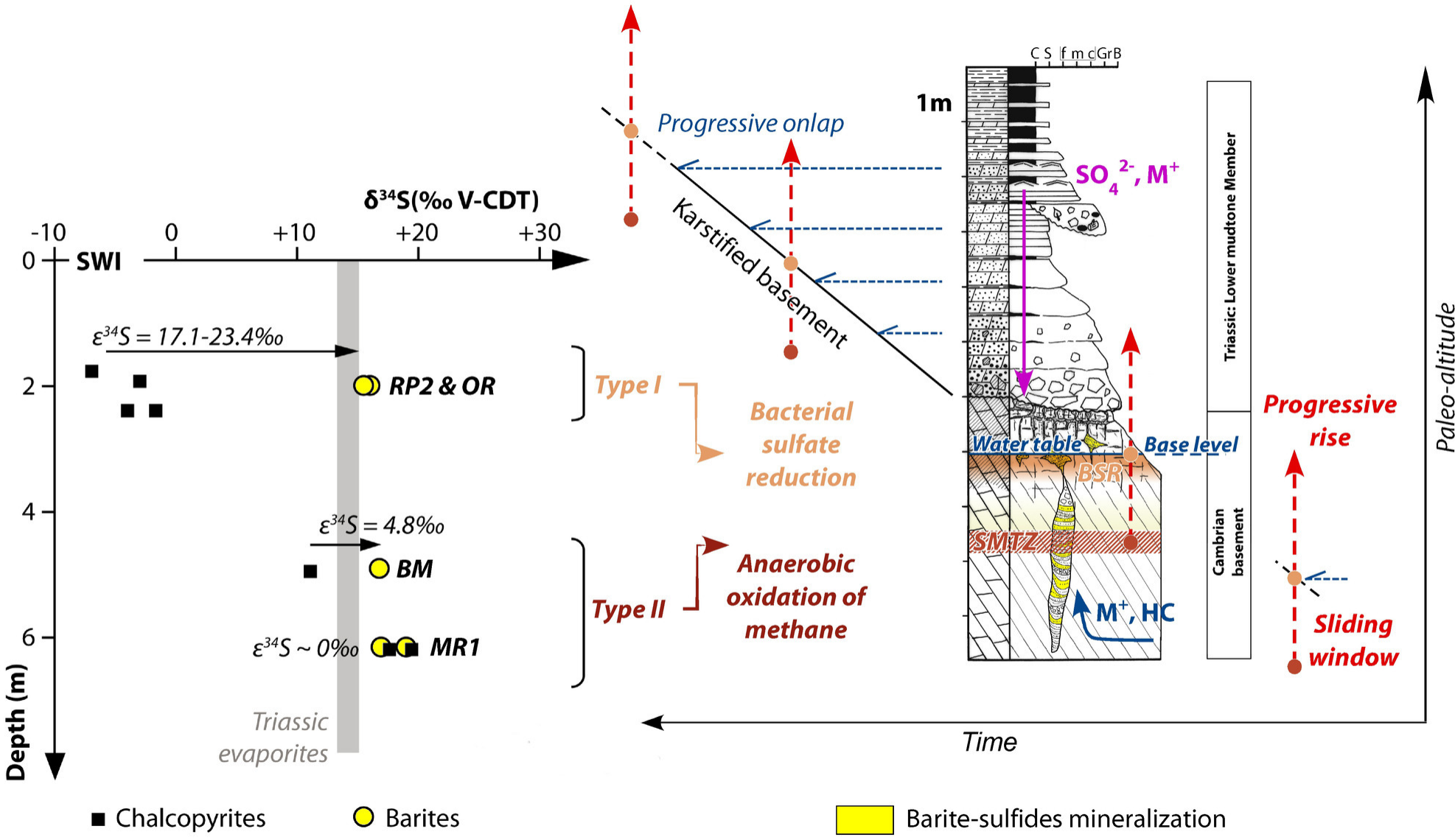
δ34S(‰ V-CDT)
-10
0
+10
+20
+30
SWI
Depth (m)
0
2
4
6
ε34S = 17.1-23.4‰
RP2 & OR
ε34S = 4.8‰
BM
ε34S ~ 0‰
MR1
Triassic evaporites
Type I
Bacterial sulfate reduction
Type II
Anaerobic oxidation of methane
Progressive onlap
Karstified basement
C S f m c GrB
1m
SO4 2-, M+
Water table
Base level
BSR
SMTZ
M+, HC
Triassic: Lower mudtone Member
Cambrian basement
Progressive rise
Sliding window
Paleo-altitude
Time
Chalcopyrites
Barites
Barite-sulfides mineralization

Stage 1:
Intense weathering and epigenic karstification

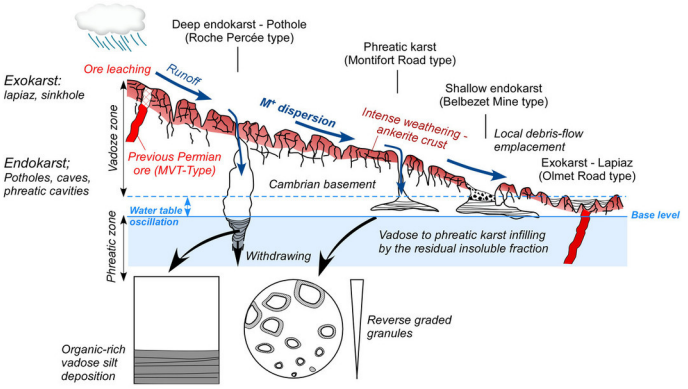

Stage 2:
Initial fringing alkaline playa-lake
Silica partial leaching and silicifications

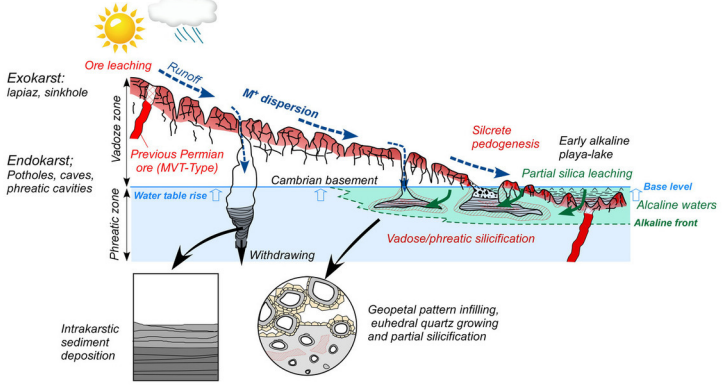

Stage 3:
Permanent sulfate-rich shallow-lake - Barite and sulfides trapping

Coeval gravity-driven synsedimentary ore trapping upstream (Type I mineralization) and early burial hydrothermal-driven trapping downstream (Type II mineralization).

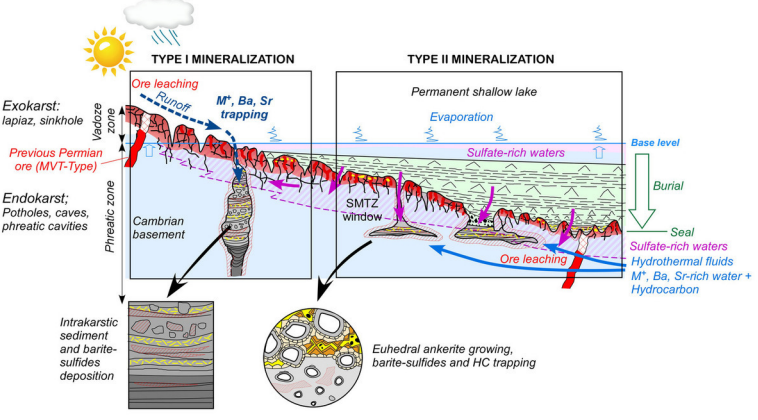

Location	Textural facies	Host mineral	Primary fluid inclusion	Te (°C)	TmIce (°C)	Th (°C)	Mean salinity (wt.%eq.NaCl)
Montifort Road	MR1	Barite (N=23)	Two-phase	-28 to -21	-15 to -5	48 to 102	13.56
		Barite	Single-phase				
Montifort Road	MR2	Barite (N=13)	Two-phase	-28 to -21	-13 to -5	139 to 195	12.6
Roche Percée Olmet Road	RP2 OR	Barite	Single-phase				

Location	Textural facies	Host mineral	$^{87}Sr/^{86}Sr$	Sr (ppm)	$\delta^{34}S$ (‰ V-CDT)
Middle Triassic ore deposits					
Roche Percée	RP2	Barite	0.708880	11850.29	+16.2
		Chalcopyrite			-2.1 -1.4
Olmet Road	OR	Barite			+15.7
		Chalcopyrite			-7.2 -1.7
Belbezet Mine	BM	Barite	0.711419	4412.85	+16.2/+16.7
		Chalcopyrite			+11.9 +17.1
Montifort Road	MR1	Barite	0.711386	10739.52	+16.9/+18.5
		Chalcopyrite			+18.9
Triassic evaporites					
Quarry of Notre Dame de Capimont	EV1	Gypsum			+13.7 +14.7
Pégairolles de l'Escalette (drillcore)	EV2	Anhydrite			+14.6 +14.9
Late Permian ore deposits *(compilation from Laurent, 2015 and Laurent et al., 2017)*					
1st mineralizing phase		Barite	0.711913 0.711826	42192.21 27764.87	+17.2/+17.6 +15.6/+16.9
		Chalcopyrite			-15
2nd mineralizing phase		Barite	0.711014 0.710936 0.710471 0.710637 0.711222	37413.52 43803.11 21466.55 19500 42225.3	+17.3/+17.9 +16.6/+16.8 +16/+16.4 +17.5 +17.8/+18.4
		Chalcopyrite			-10 -13 -6/-5
3rd mineralizing phase		Barite	0.710000 0.710081 0.710294 0.710003	43855.8 32585.4 28491.79 28964.38	+16.4/+17.2 +16.1/+16.9 +16.2/+16.7 +17
		Chalcopyrite			-12/-11 -8